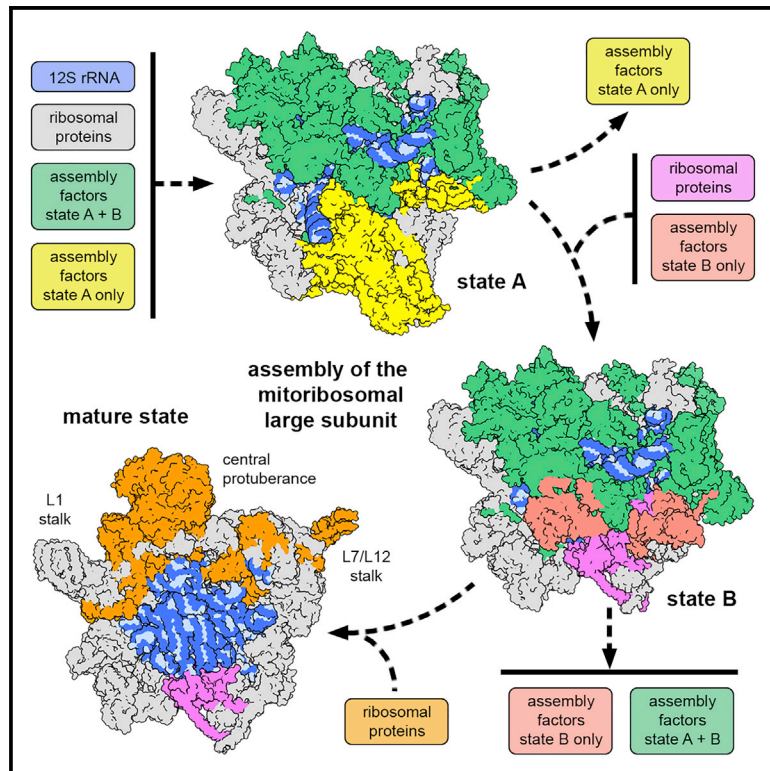


Structural Insights into the Mechanism of Mitoribosomal Large Subunit Biogenesis

Graphical Abstract



Authors

Mateusz Jaskolowski,
David J.F. Ramrath, Philipp Bieri, ...,
Daniel Boehringer, André Schneider,
Nenad Ban

Correspondence

andre.schneider@dcb.unibe.ch (A.S.),
ban@mol.biol.ethz.ch (N.B.)

In Brief

The structures of two assembly intermediates of the *Trypanosoma brucei* mitoribosomal large subunit in combination with biochemical analysis provide insights into the stepwise mitoribosomal biogenesis process that involves numerous assembly factors functioning as enzymes or scaffold components.

Highlights

- Assembly intermediates of the mitoribosomal large subunit resolved by cryo-EM
- Network of interactions between the GTPases mt-EngA, Mtg1, and mt-EngB revealed
- Partially immature 12S rRNA is stabilized by numerous assembly factors
- Ribosomal biogenesis involves exchange of assembly factors by ribosomal proteins

Article

Structural Insights into the Mechanism of Mitochondrial Large Subunit Biogenesis

Mateusz Jaskolowski,^{1,3} David J.F. Ramrath,^{1,3} Philipp Bieri,^{1,3} Moritz Niemann,^{2,3} Simone Mattei,¹ Salvatore Calderaro,² Marc Leibundgut,¹ Elke K. Horn,² Daniel Boehringer,¹ André Schneider,^{2,*} and Nenad Ban^{1,4,*}

¹Department of Biology, ETH Zurich, Zurich 8093, Switzerland

²Department of Chemistry and Biochemistry, University of Bern, Bern 3012, Switzerland

³These authors contributed equally

⁴Lead Contact

*Correspondence: andre.schneider@dcb.unibe.ch (A.S.), ban@mol.biol.ethz.ch (N.B.)

<https://doi.org/10.1016/j.molcel.2020.06.030>

SUMMARY

In contrast to the bacterial translation machinery, mitochondrial ribosomes and mitochondrial translation factors are highly divergent in terms of composition and architecture. There is increasing evidence that the biogenesis of mitochondrial ribosomes is an intricate pathway, involving many assembly factors. To better understand this process, we investigated native assembly intermediates of the mitochondrial large subunit from the human parasite *Trypanosoma brucei* using cryo-electron microscopy. We identify 28 assembly factors, 6 of which are homologous to bacterial and eukaryotic ribosome assembly factors. They interact with the partially folded rRNA by specifically recognizing functionally important regions such as the peptidyltransferase center. The architectural and compositional comparison of the assembly intermediates indicates a stepwise modular assembly process, during which the rRNA folds toward its mature state. During the process, several conserved GTPases and a helicase form highly intertwined interaction networks that stabilize distinct assembly intermediates. The presented structures provide general insights into mitochondrial maturation.

INTRODUCTION

Mitochondria are cellular organelles responsible for energy conversion and ATP production. They originated from a free-living α -proteobacterium, and therefore share a common ancestor with present-day bacteria (Roger et al., 2017). Although during evolution, the majority of the genetic information has been either lost or transferred from the mitochondrial to the nuclear genome, mitochondria have retained their own transcription and translation machineries, including mitochondrial ribosomes (mitochondrial ribosomes). In all known organisms, mitochondrial ribosomes are responsible for the synthesis of essential membrane proteins of the oxidative phosphorylation complexes (Ott et al., 2016).

Despite sharing a common ancestor, mitochondrial ribosomes differ considerably in composition and architecture from their bacterial counterparts and between different eukaryotic lineages, as recently visualized at high resolution by cryo-electron microscopy (cryo-EM). In general, mitochondrial ribosomes feature an increased number of ribosomal proteins in comparison to the bacterial 70S ribosome, whereas the ribosomal RNAs (rRNAs) are highly variable in length. The rRNAs of the yeast 74S mitochondrial ribosome developed additional expansion segments to which mitochondrial-specific proteins bind, leading to an RNA:protein ratio of 1:1 (2:1 in bacteria) (Desai et al., 2017). In contrast, the mammalian 55S mitochondrial ribosome possesses a highly reduced rRNA, but ac-

quired additional mitochondria-specific ribosomal proteins, resulting in an RNA:protein ratio of 1:2 (Amunts et al., 2015; Greber et al., 2015). The *Trypanosoma brucei* mitochondrial ribosome is the utmost example of this evolutionary shift toward protein-based architecture, as it is composed of 127 mitochondrial proteins and contains very small rRNAs, resulting in an RNA:protein ratio of 1:6 (Ramrath et al., 2018).

Considering the unique architecture of mitochondrial ribosomes and the fact that rRNA transcription occurs inside the mitochondrion, whereas most mitochondrial proteins are synthesized in the cytoplasm and must be imported, the biogenesis of mitochondrial ribosomes is expected to differ from the assembly of prokaryotic and eukaryotic cytoplasmic ribosomes. However, in contrast to the cytoplasmic ribosomes, whose biogenesis has been studied extensively for decades using genetic, biochemical, and structural approaches (Chen and Williamson, 2013; de la Cruz et al., 2015; Davis et al., 2016; Klinge and Woolford, 2019; Shajani et al., 2011; Woolford and Baserga, 2013), the maturation of mitochondrial ribosomes is less well understood. Only a few mitochondrial assembly factors have been identified so far, including rRNA methyltransferases (Mrm1, Mrm2, and Mrm3), ATP-dependent RNA helicases (Mss116 and Mrh4), and GTPases (Mtg1, Mtg2, and Mtg3) (reviewed in De Silva et al., 2015). For the mammalian 28S and 39S subunits, an assembly hierarchy of their mitochondrial proteins has recently been proposed using stable isotope

labeling with amino acids in cell culture (SILAC) pulse-labeling experiments (Bogenhagen et al., 2018). At the same time, an assembly pathway of mitochondrial proteins was suggested for the yeast 54S large subunit (LSU) using a systematic genomic deletion of 44 yeast mitochondrial proteins (Zeng et al., 2018). Both studies showed that, similar to the bacterial LSU (Davis et al., 2016), the mitochondrion is assembled through stepwise association of clusters of ribosomal proteins.

Structural insights into mitochondrial assembly are limited to studies in which assembly intermediates of the *T. brucei* mitochondrial small subunit (SSU) were described (Saurer et al., 2019), and the observation of two late-stage assembly intermediates of the human 39S LSU (Brown et al., 2017). The latter showed that maturation of the peptidyltransferase center (PTC) formed by the 16S rRNA and the binding of bL36m are among the last steps in human mitochondrial LSU maturation. Cryo-EM reconstructions described in that study also revealed a module consisting of three assembly factors (MALSU1, LOR8F8, and mt-ACP) that binds to uL14m and prevents premature subunit association.

Mitochondrial biogenesis is biomedically important since mutations in mitochondrial proteins, rRNAs, and assembly factors have been linked to a heterogeneous group of human multisystemic oxidative phosphorylation (OXPHOS) diseases and cancer development and progression (Kim et al., 2017; De Silva et al., 2015). Furthermore, a mammalian ortholog of the recently identified yeast mitochondrial assembly factor Mam33 is a protein involved in cancer progression and mitochondrial diseases (Hillman and Henry, 2019).

Here, we present the atomic structures of two native *T. brucei* mitochondrial LSU assembly intermediates determined by cryo-EM at resolutions of 3.1 and 3.9 Å. The intermediates feature 12S rRNAs in immature conformations and vary in the number of bound mitochondrial proteins and biogenesis factors, suggesting a sequential order of assembly. We discover many novel assembly factors in addition to those with homology to previously biochemically characterized biogenesis factors of other systems. Moreover, we visualize the mode of interaction of the assembly factors with the immature mitochondrion. Finally, we present the conformational changes that occur during the maturation of mitochondria and the roles of various factors in this process.

RESULTS

Cryo-EM Analysis of Trypanosomal Mitochondria Reveals Two Native Assembly Intermediates of the LSU

Mitochondrial particles were purified from wild-type *T. brucei* cells and analyzed using cryo-EM. Two complexes that are structurally related to the ribosomal LSU, referred to as states A and B, could be classified from the dataset (Figures 1 and S1). The cryo-EM maps were resolved to 3.9 and 3.1 Å (Figure S2), respectively, and were of sufficient quality for building and refining an atomic model for both states according to the previously described strategy (Ramrath et al., 2018) (Table 1).

Several lines of evidence indicate that the visualized complexes represent large mitochondrial subunit assembly intermediates. Both complexes lack the central protuberance (CP) (Fig-

ure 1A), a prominent architectural feature that is responsible for intersubunit contacts with the SSU, which is known to be formed late during bacterial large ribosomal subunit biogenesis (Davis et al., 2016). Furthermore, a highly intertwined cluster of non-ribosomal proteins is located on the subunit interface side of both complexes (Figures 1A and 1B). The protein cluster interacts with mitochondrial proteins and the central core of the LSU formed by the 12S rRNA that harbors the PTC found in immature conformation. Whereas the intersubunit side is almost completely covered, the solvent-accessible side resembles the previously published subunit (Ramrath et al., 2018). The L1 stalk, involved in tRNA release at the exit site, lacks mitochondrial proteins mL91 and mL97 in both states. In the mature LSU, these proteins are located at the base of the L1 stalk, ensuring its correct positioning and solid attachment to the LSU. Although in the L1 stalk only 2 ribosomal proteins are missing, the L7/L12 stalk is completely absent in both states, along with many of the stalk base mitochondrial proteins, in particular, uL10m, uL16m, bL36m, and mL88. Furthermore, both states lack mL79, which links the CP with the stalk base in the mature LSU. Additional nearby proteins, mL64 and mL84, although present in both complexes, adopt different, immature conformations. In total, states A and B lack 22 and 17 mitochondrial proteins, respectively, out of the 72 found in the mature LSUs.

Overall, of the 25 additional proteins identified in state A and the 21 in state B, 16 are present in both states (Figures 1B and S3). Some of these proteins are structural homologs of previously described mitochondrial or cytoplasmic ribosomal assembly factors, including bacterial GTPases EngA (Bharat et al., 2006) and EngB (Schaefer et al., 2006), rRNA methyltransferase RlmI (Purta et al., 2008), mitochondrial GTPase Mtg1 (Barrientos et al., 2003), mitochondrial rRNA methyltransferase MRM3 (Rorbach et al., 2014) and mitochondrial RNA pseudouridine synthase Pus5/RPUSD4 (Ansmant et al., 2000; Antonicka et al., 2017), as well as the acyl carrier protein (ACP) leucine-tyrosine-arginine motif (LYRm) module recently identified in human mitochondrial LSU assembly intermediates (Brown et al., 2017). Consequently, we assigned the newly identified proteins as assembly factors and refer to them as mitochondrial LSU assembly factors (mt-LAFs). Assembly factors with previously characterized homologs were named with their original name and an “mt-” prefix. To corroborate their functional role in ribosome maturation, a selection of the newly found assembly factors was further tested using RNA interference (RNAi) knock-down experiments, which showed that their ablation interferes with LSU maturation (Figure 2).

Comparison of the Assembly Intermediates Suggests the Order of Maturation

In both assembly intermediates, the intertwined assembly factors stabilize the 12S rRNA in an immature conformation (Figure 1). Domain II, namely helices 36–37, 39, and 42–44, and domain V that forms the PTC in the mature LSU, are present in the same immature conformation in both states. However, helices 33–35 of domain II, the entire domain III and helices 61 and 64 of domain IV differ between the 2 assembly intermediates (Figure 1C). In state A, those rRNA regions are supported by a cluster of 9 assembly factors, including mt-LAF21 and KRIPP3,

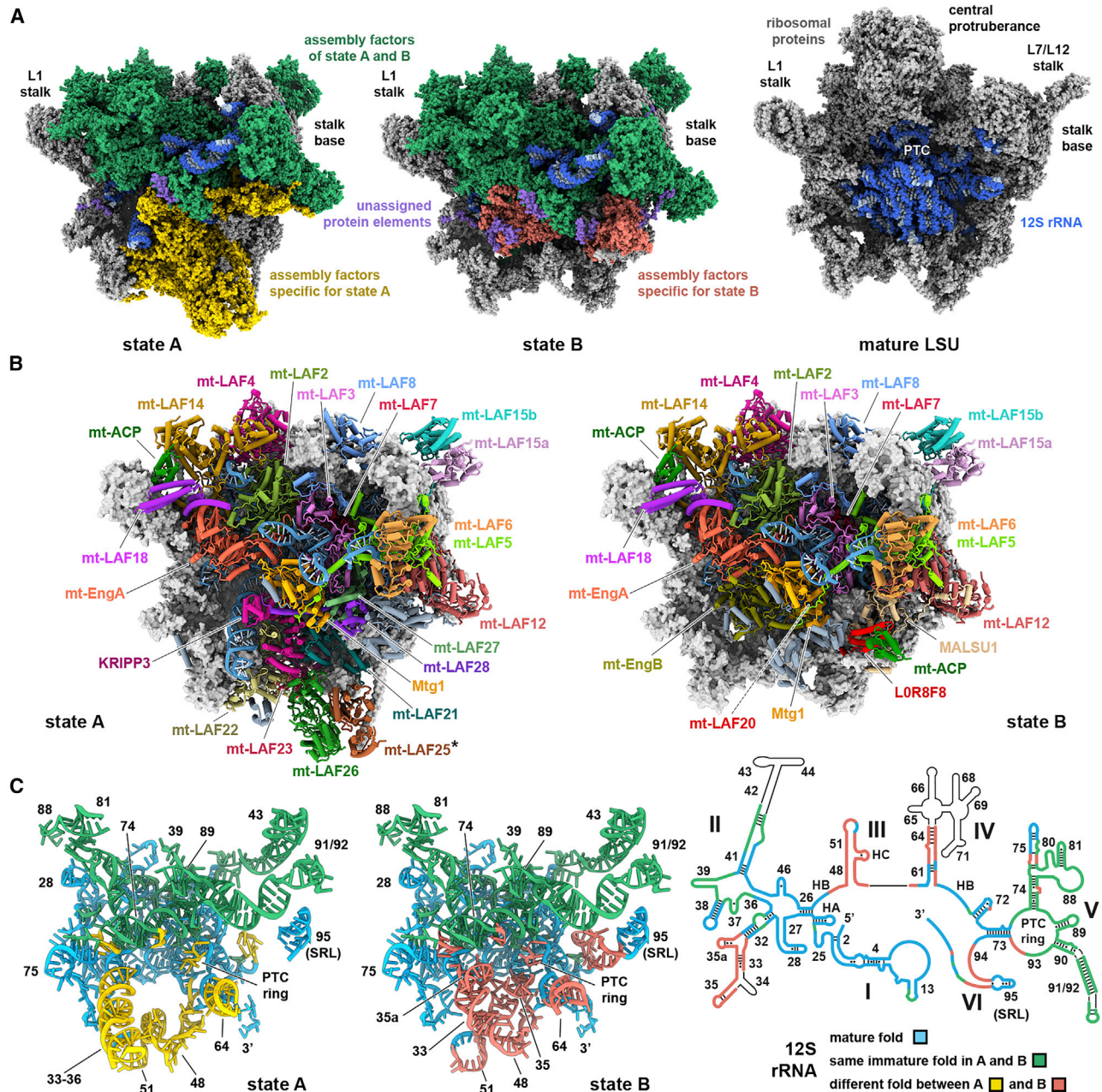


Figure 1. Architectural Overview of the Mitribosomal LSU Assembly Intermediates of *T. brucei*

(A) The molecular structures of the mitribosomal LSU state A and state B assembly complexes are shown in sphere representation from the intersubunit side. For comparison, the LSU of *T. brucei* (PDB: 6HIX) (Ramrath et al., 2018), including a modeled 12S rRNA, is shown.

(B) The assembly factors of states A and B are illustrated and colored individually. The model of the 12S rRNA is blue. The ribosomal proteins are shown as gray surfaces. mt-LAF20 in state B is labeled with a dashed line, as it is occluded from view by other assembly factors. mt-LAF25* lacks an assigned sequence, but based on fold homology represents a putative methyltransferase.

(C) The 12S rRNA structures of states A and B are shown from the intersubunit side (same orientation as in A and B). The 12S rRNA segments, some of which are labeled, are colored according to their conformational state: mature elements in blue, immature elements with the same fold in states A and B in green, and elements adopting conformations specific for state A in yellow and for state B in red, respectively. The 12S rRNA secondary structure diagram of state B is given in the same color key.

which bind between domains II, III, and IV. Consistent with the important structural role of these factors in stabilizing rRNA domains in immature conformation, knockdowns of mt-LAF21

and KRIPP3 specifically reduce the steady-state levels of 12S rRNA. In contrast, the SSU 9S rRNA is not affected, suggesting that the targeted protein is required for LSU but not SSU

Table 1. Cryo-EM Data Collection, Map Refinement, Model Refinement, and Validation Statistics of the *T. brucei* mt-LSU Assembly Intermediates

Structure	State A mt-LSU Assembly Intermediate	State B mt-LSU Assembly Intermediate
EMDB accession/PDB code	EMDB: 10999 / PDB: 6YXX	EMDB: 11000 / PDB: 6YXY
Data Collection		
Microscope	FEI Titan Krios	
Detector	Falcon 3	
Voltage (keV)	300	
Electron exposure (e ⁻ /Å ²)	75	
Pixel size (Å)	1.085	
Magnification	129,000×	
Defocus range (μm)	1–3	
Automation software	EPU	
Selected micrographs	26,776	
EM Reconstruction		
Initial particle images (no.)	2,480,610	
Final particles (no.)	16,215	98,508
Accuracy of rotations (°)	0.722	0.411
Accuracy of translations (Å)	0.915	0.487
Resolution (unmasked/masked) at FSC = 0.143 (Å)	3.9	3.1
Sharpening B factor (Å ²)	–153.93	–128.35
Coordinate Real-Space Refinement (PHENIX Version 1.17.1-3660)		
Unit cell	P1	P1
a, b, c (Å)	260.40, 324.05, 292.23	258.23, 321.16, 294.04
α = β = γ (°)	90	90
CC _{mask}	0.76	0.81
High-resolution limit for refinement	3.9	3.1
Resolution according to model versus map FSC = 0.143 / FSC = 0.5 (masked) criteria (Å)	3.8/3.9	3.0/3.1
Resolution according to model versus map FSC = 0.143 / FSC = 0.5 (unmasked) criteria (Å)	3.9/4.0	3.0/3.2
Model Composition		
No. of chains	96	94
Total atoms	183,960	177,572
Protein residues	29,866	19,399
RNA residues	906	903
Ligands: GTP/ATP/NAD/SPD/PM8/H ₂ O/Na ⁺ /Mg ²⁺ /Zn ²⁺	2/1/1/–/1/8/2/17/7	3/1/1/1/2/10/2/33/5
Average B Factors (min/max/mean)		
Protein	5.49/115.83/33.55	3.34/90.08/27.12
RNA	4.28/261.05/63.34	4.95/175.21/45.28
Ligand	1.89/98.95/57.77	5.40/96.97/51.22
Water	13.94/57.01/33.98	9.39/38.53/19.00
Model Validation		
RMSD bonds (Å)	0.002	0.002
RMSD angles (°)	0.468	0.460
All-atom clashscore	9.26	7.78
EMRinger score	1.14	2.35
MolProbity score	1.64	1.66

(Continued on next page)

Table 1. Continued

Structure	State A mt-LSU Assembly Intermediate	State B mt-LSU Assembly Intermediate
Ramachandran Statistics		
Favored (%)	97.17	99.17
Allowed (%)	2.82	2.82
Outliers (%)	0.01	0.01
Rotamer outliers (%)	0.95	1.29
RNA Validation		
Sugar pucker outliers (%)	0.33	1.22
Angle/bond outliers (%)	0	0
Bond outliers (%)	0	0

CC_{mask}, real space correlation coefficients; EMDB, *Electron Microscopy Data Bank*; FSC, X; PDB, Protein Data Bank; RMSD, root-mean-square deviation; SPD, spermidine, FSC., Fourier shell correlation

maturation. Furthermore, the growth rate of *T. brucei* cells is reduced, presumably due to retarded mitoribosome assembly (Figure 2A and S3C). In state B, the cluster of 9 assembly factors specific to state A is replaced by 4 mitoribosomal proteins (mL90, mL99, mL100, and mL101) and by the assembly factors mt-LAF20 and mt-EngB, a homolog of the bacterial GTPase EngB (Schaefer et al., 2006) (Figures 1A and 1B). The exchange of proteins is accompanied by a conformational change of the N terminus of the mL85 and 12S rRNA regions, which in state B adopt a fold more similar to the one found in mature LSU. In addition, we observe differences between the two assembly intermediates in the vicinity of H95, called the sarcin-ricin loop (SRL). While in state A, this rRNA region is occupied by protein secondary structure elements that could not be assigned due to lower local resolution; in state B different proteins are bound to the SRL, including mitoribosomal protein uL14m and 3 assembly factors—MALSU1, LOR8F8, and ACP—that belong to a module that was recently shown to be involved in the maturation of the human mitoribosome (Brown et al., 2017). The exchange of proteins is accompanied by a maturation of the nearby H94. Since state B has a more complete set of ribosomal proteins and the fold of its rRNA resembles more closely the one present in the mature LSU, we propose that this state represents a later assembly intermediate than state A.

GTPases Form a Network of Interactions

Studies on ribosomal biogenesis suggest that GTPases are frequently engaged in ribosomal maturation and may couple the ribosome assembly with growth control pathways by sensing the cellular GTP/GDP level (Britton, 2009). The structures of the mitoribosomal LSU assembly intermediates contain several GTPases in agreement with previous biochemical evidence that GTPases also play an important role in mitoribosome biogenesis (Gupta et al., 2018; Kotani et al., 2013). The identified GTPases mt-EngA·GTP₂ and Mtg1, as well as mt-EngB·GTP, which is present only in state B, are homologous to GTPases known to be involved in ribosome biogenesis in bacteria (Schaefer et al., 2006; Uicker et al., 2006). All three of these GTPases are located at the center of the LSU and interact with key elements of the 12S rRNA (Figure 3A). In state A, GTPase mt-EngA·GTP₂ and

Mtg1 interact with each other and form a docking site for the cluster of assembly factors that are only present in state A. During transition to state B, this cluster is replaced by a set of mitoribosomal proteins and the assembly factors mt-LAF20 and the GTPase mt-EngB·GTP.

Simultaneous binding of these three GTPases to an assembly intermediate is consistent with the evidence that suggests that homologs of mt-EngA·GTP₂, Mtg1, and mt-EngB·GTP work in conjunction during the bacterial LSU maturation (Ni et al., 2016). Although there is at present no structure of these GTPases bound simultaneously to the bacterial large ribosomal subunit, structures of EngA in complex with mature *Escherichia coli* 50S LSU (Zhang et al., 2014) and Mtg1 homolog, RbgA, bound to *Bacillus subtilis* 45S assembly intermediate (Seffouh et al., 2019) are available. We used this information to create a schematic of prokaryotic 45S assembly intermediates in complex with both GTPases (Figure 3B). The observed mode of binding of the trypanosomal mt-EngA·GTP₂ and Mtg1 to the mitochondrial LSU assembly intermediate resembles very closely the composite binding mode assumed for its prokaryotic homologs (Figures 3A and 3B). Therefore, it is tempting to assume that the lessons learned regarding the interplay of these three GTPases based on the structures presented here will also be applicable to understanding the maturation of bacterial ribosomes.

The mt-EngA·GTP₂ is a homolog of the bacterial GTPase EngA (also known as Der), which is an essential and conserved bacterial 50S maturation factor (Hwang and Inouye, 2006). As in bacteria, mt-EngA·GTP₂ consists of 2 consecutive GTPase domains (G1 and G2) followed by a C-terminal RNA-binding KH domain. Although the binding environment in the trypanosomal mitoribosome is dominated by proteins instead of rRNA, the overall conformation and binding location of mt-EngA is similar to the bacterial EngA in complex with the mature bacterial 50S (Zhang et al., 2014). The binding of mt-EngA·GTP₂ interferes with the association of mL91 and bL33m, as is observed for the latter protein in bacterial ribosomes. The G1 domain binds the helical N terminus of mL74, stabilizing its immature conformation, and interacts with the immature H88 of the 12S rRNA. The G2 domain attaches to the flipped-out nucleotides of H75, a central helix of the rRNA

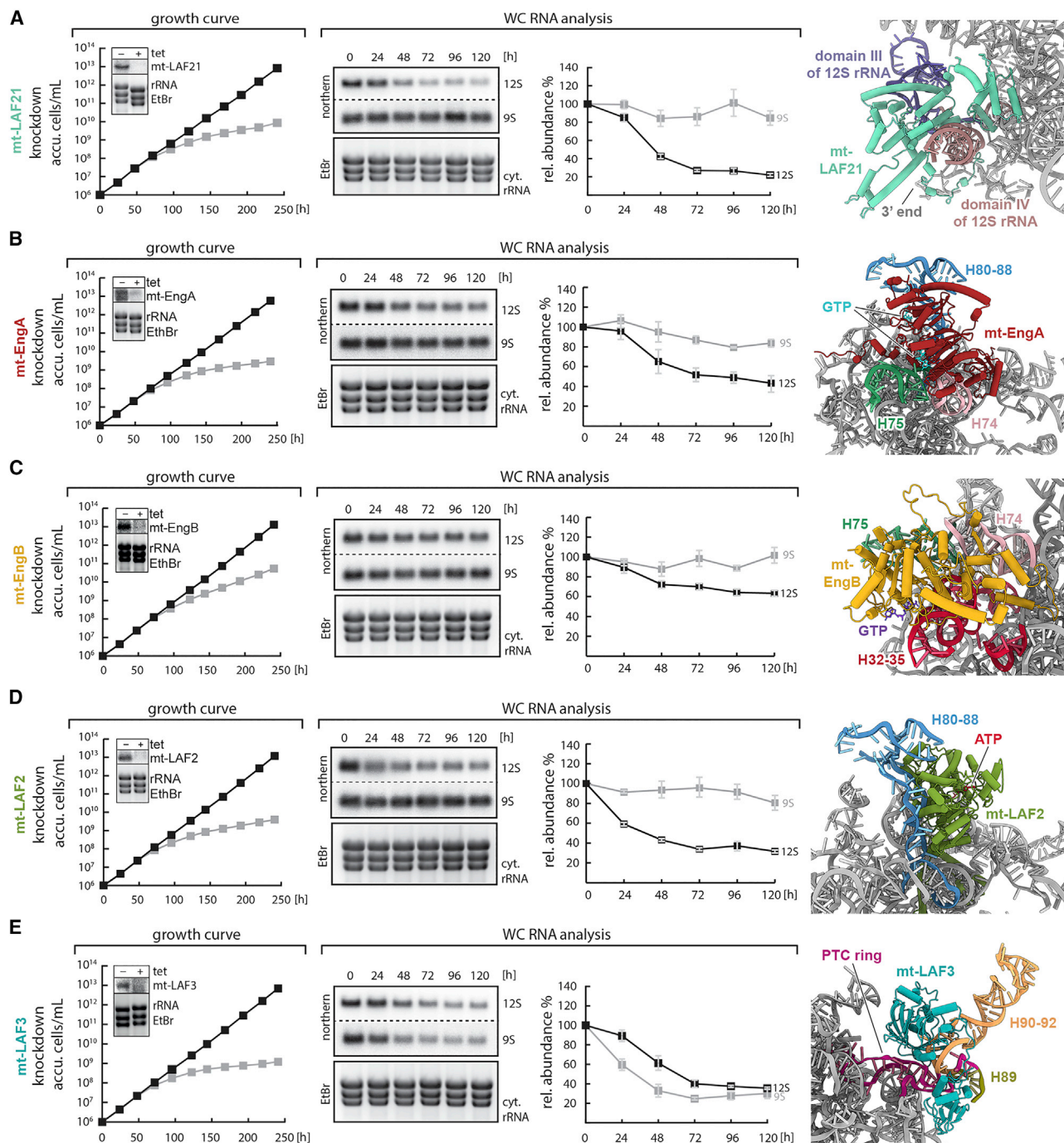
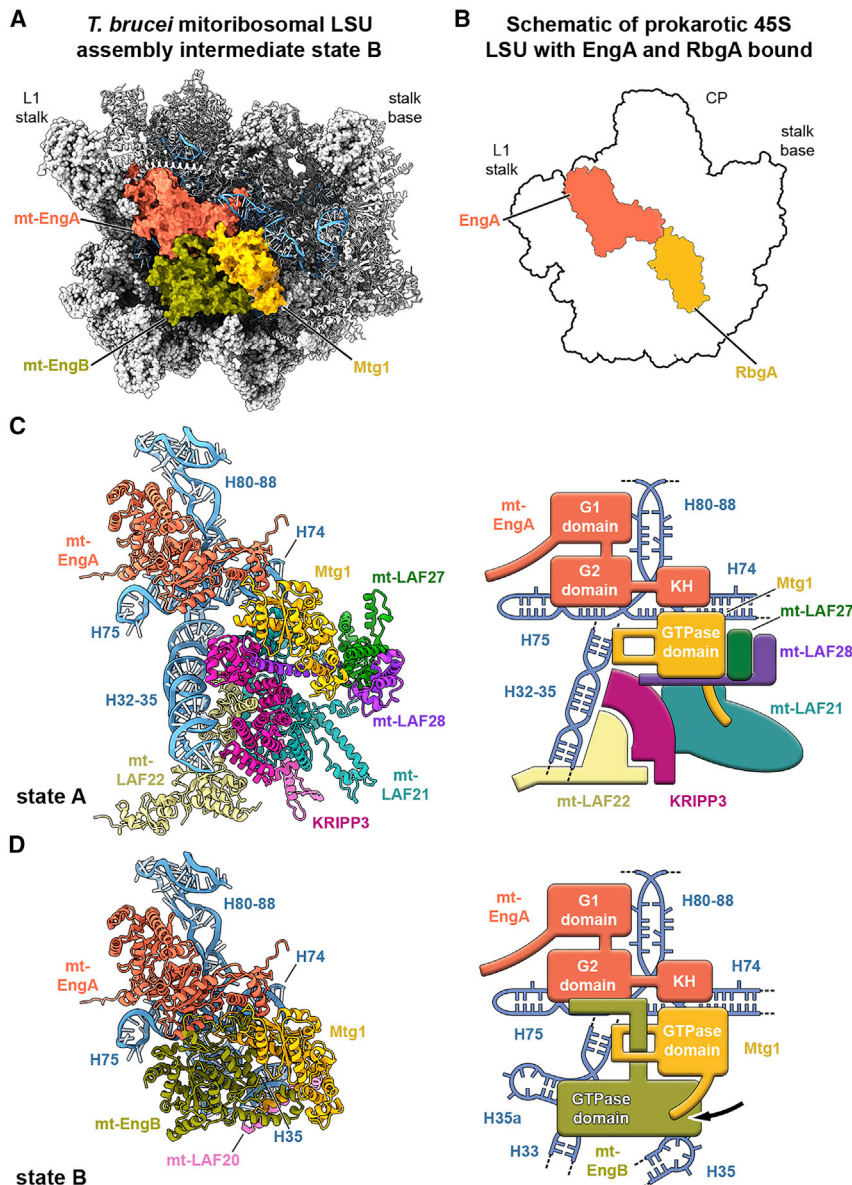


Figure 2. Importance of Assembly Factors for Cell Growth and rRNA Stability

The protein levels of five assembly factors (A–E) of the LSU assembly intermediate were reduced by tetracycline-inducible RNAi in *T. brucei* cells. All knockdown cultures show reduced growth 72 h after induction. The levels of 12S and 9S rRNA in the knockdown strains were followed in 24-h intervals by northern blotting, and with the exception of mt-LAF3 (E), all show a specific reduction of the 12S rRNA steady-state level, but not of the 9S rRNA. Ribosomal proteins of the LSU and SSU (see Figure S3) are used as controls. The results complement previous findings regarding the mitochondrial SSU assembly machinery (Saurer et al., 2019). The structures of the assembly factors from state B are shown together with their corresponding rRNA interaction sites. The structure of mt-LAF21 (A) was taken from state A, as it is specific to that state. Cultures were grown in triplicates. Error bars indicate the average deviation from the mean. See also Figure S3.



core, and orients the KH domain to contact the helix 89 of the partially formed PTC. On the opposite end, the N-terminal tail of mt-EngA anchors the factor to the base of the L1 stalk (Figure 3). In *E. coli*, only GTP-bound EngA interacts with the LSU intermediate in the late state of maturation (Tomar et al., 2009). This may also be the case for mt-EngA·GTP₂ since our cryo-EM maps reveal that GTP molecules are present in the binding pocket of both GTPase domains of mt-EngA·GTP₂ (Figure S4A). The importance of mt-EngA·GTP₂ in LSU maturation is further emphasized by the fact that *T. brucei* cells grow much slower when mt-EngA·GTP₂ is knocked down, and we observed a reduction of the 12S rRNA steady-state levels 72-h post-induction by >60% (Figure 2B).

The conserved Mtg1 binds at the subunit interface side, where it interacts with the KH domain of mt-EngA, many other LAFs,

Figure 3. GTPases Form an Intricate Network of Interactions

(A) State B assembly intermediate of the *T. brucei* mitoribosomal LSU with the assembly factor GTPases mt-EngA, mt-EngB, and Mtg1 shown in colored surface representation and the rRNA in blue.

(B) Schematic representation of the binding locations of prokaryotic GTPases RbgA and EngA to the prokaryotic 45S LSU assembly intermediate based on separate structures of 45S:RbgA (PDB: 6PPK) and 50S:EngA (PDB: 3J8G).

(C and D) The silhouettes of the assembly intermediate states A (C) and B (D) are shown from the intersubunit side as black outlines in the same orientation as in (A). mt-EngA, mt-EngB, and Mtg1, as well as the other assembly factors mt-LAF20, mt-LAF21, mt-LAF22, KRIPP3, mt-LAF27, and mt-LAF28, are involved in the rearrangement of the H32–35 region. Regions of the 12S rRNA that interact with the GTPase cluster (H74, H75, H80–88, and H32–35 regions) are shown in blue, while the remaining 12S rRNA is omitted for clarity. Corresponding schematic representations of the GTPase clusters in states A and B are shown at right. mt-LAF20 is not shown on the state B schematic, as it is occluded from view by EngB and Mtg1. The conformational change of the N terminus of Mtg1 between states A and B is indicated by an arrow. See also Figures S4A and S4B.

12S rRNA, and a few mitoribosomal proteins, including uL14m (Figure 3). The observed binding location and the state of assembly in which the LSU is lacking proteins uL16m, bL27m, and bL36m is consistent with the data available for the binding of the prokaryotic homolog of Mtg1, called RbgA (or YlqF), to the immature 50S subunit (Jomaa et al., 2014; Matsuo et al., 2006; Seffouh et al., 2019). Although the active site residues of Mtg1 responsible for the nucleotide binding and hydrolysis are conserved (Gulati et al., 2013), we find the binding pocket in

a conformation that prevents binding of a nucleotide due to steric hindrance, implying that Mtg1 in our assembly intermediates serves an architectural role, whereas its nucleotide bound state may be required for LSU assembly at another stage of maturation, as proposed earlier (Kim and Barrientos, 2018). Therefore, the observed conformational changes of Mtg1 between the 2 assembly intermediates (Figure 3) do not involve the GTPase domains but are mostly limited to the N-terminal helix of the factor, which rotates by 90° when the cluster of assembly factors specific for state A dissociates.

Upon the dissociation of state A-specific factors, mt-EngB·GTP is recruited, a homolog of the bacterial GTPase EngB (also known as YihA or YsxC). The contacts between the two GTPases involve the rotated N-terminal helix of Mtg1 and the trypanosomal specific long C-terminal extension

(CTE) of mt-EngB·GTP, which threads through a loop formed by Mtg1, establishing a shared β -sheet. mt-EngB·GTP knockdown experiments showed a reduced cell growth phenotype in trypanosomes and a 40% reduction of the 12S rRNA steady-state levels after 96 h of RNAi induction (Figure 2C). We observed a nucleotide bound to the GTPase domain of mt-EngB·GTP (Figure S3B) in the same location as observed in the crystal structure of GMP-PNP-bound bacterial homolog YsxC (Ruzhenikov et al., 2004).

Due to the structural homology to bacterial factors, the observed contacts between mt-EngA·GTP₂ and Mtg1 are likely also formed during bacterial large ribosomal subunit biogenesis. This is not the case for the contacts between GTPases that are mediated by the unique CTE of mt-EngB·GTP, and therefore, it is possible that in bacteria, the communication between EngB and other GTPases is facilitated by the structural changes in the LSU during maturation. Nevertheless, the observed intricate network of interactions may provide an example of how these GTPases are able to coordinate their action to function as checkpoint proteins in the assembly process (Britton, 2009).

mt-LAF2 Is a DEAD-Box Helicase that Interacts with the 12S rRNA

mt-LAF2·ATP, the largest of the identified assembly factors (85.6 kDa, 754 amino acids [aa]), is a member of the DEAD-box helicase family and consists of 2 highly conserved RecA-like domains, which harbor the DEAD-box motif (Fairman-Williams et al., 2010). The RecA-like domains exhibit a closed conformation, which for bacterial DEAD-box helicase YxiN has been shown to be induced by a cooperative binding of RNA and an ATP molecule (Theissen et al., 2008). Located below the CP region, the RecA-like domains interact with 12S rRNA elements of H37, H39, and H80-81 and with assembly factors. They overlap with the binding location of many mitochondrial proteins, some of them being part of the CP in the mature LSU, including bL27m, bL31m, and bL33m. As observed in other DEAD-box helicases (Putnam and Jankowsky, 2013), mt-LAF2·ATP contains terminal extensions, which in trypanosomal LSU assembly intermediates intertwine with the 12S rRNA core (Figure 4A). The C-terminal tail is particularly long (164 aa) and extends through the entire core of the complex, thereby blocking the entry to the lower part of the polypeptide exit tunnel. mt-LAF2·ATP also contains an additional domain between the two RecA-like domains, which is uncommon for DEAD-box helicases (Figure 4B) (Fairman-Williams et al., 2010). This domain is positioned in front of the nucleotide-binding pocket and is stabilized through interactions with mt-LAF3 and mt-LAF8 (Figure S5C). Thus, this interaction may prevent the dissociation of bound nucleotide and subsequent conformational change of mt-LAF2 as long as mt-LAF3 and/or mt-LAF8 stay bound to the assembly intermediate in the current conformation.

Considering that mt-LAF2·ATP is deeply buried in the core of the assembly intermediate and is highly intertwined with the 12S rRNA (Figure S5B), it is likely that it is recruited early in the maturation. The 12S rRNA steady-state levels drop rapidly to 60% after 24-h post-induction and to 40% after 48-h post-induction in mt-LAF2·ATP knockdown cells (Figure 2D), and the growth rate of the *T. brucei* cells is significantly reduced.

These results resemble the findings for Mss116, a DEAD-box helicase in yeast, which plays a role in mitochondrial maturation (De Silva et al., 2017). The deletion of Mss116 lowers the number of assembly intermediates and assembled mitochondria, suggesting an involvement at an early stage of the maturation process. Just like mt-LAF2·ATP, Mss116 also has a long CTE (Del Campo and Lambowitz, 2009), which contributes to the RNA binding (Mohr et al., 2008). Although the CTE of Mss116 adopts a compact conformation, it is possible that upon binding to the early-stage assembly intermediate, the Mss116 CTE unfolds and interacts with the rRNA similarly to the CTE of mt-LAF2·ATP described here. Our structural and biochemical results indicate that mt-LAF2·ATP, similarly to Mss116, plays an important role in the early stage of mitochondrial biogenesis and acts as a key rRNA scaffold or even as the nucleation center. In addition, it interferes with the association of the CP proteins and would have to dissociate upon CP maturation, possibly inducing a large rearrangement of the PTC rRNA core region.

Maturation of the PTC Involves Multiple Assembly Factors

In the mature ribosomal LSU, rRNA elements of domain V form the PTC, the catalytic site of the ribosome. Although the PTC region of the rRNA is not well ordered in the structure of *T. brucei* mitochondria (Ramrath et al., 2018), due to high degree of conservation it is reasonable to assume that it will adopt the conformation observed in the mature mammalian 39S LSU (Greber et al., 2015) (Figures 4C and 4D). Therefore, in the discussion below, we compare the conformation of the PTC observed in the LSU assembly intermediates to the homology modeled structure of the mature PTC. In both mitochondrial LSU assembly intermediates, the PTC regions of the 12S rRNA interact with numerous assembly factors and are in an immature conformation. In particular, H80, called the P-loop, is unwound by extensive interactions with the DEAD-box helicase mt-LAF2·ATP described above (Figure 4C), similar to that observed in several crystal structures of DEAD-box helicases in complex with RNA fragments (Del Campo and Lambowitz, 2009; Sengoku et al., 2006) (Figure S5A). Similarly, H88, which in bacteria interacts with the E-site tRNA during translation, is unwound in the LSU assembly intermediates. Instead of the canonical stem-loop structure, the rRNA segment of H88 forms a lariat-like structure that wraps around a loop of mt-LAF4 and the C-terminal helix of mL64 (also called CRIF1 in mammals). This lariat is sandwiched between a loop of mt-LAF19, the core domain of mt-LAF4, and mt-LAF14 (Figure 4C). Together, these factors prevent formation of the H88 stem-loop structure. Whereas we cannot detect proteins that are homologous to mt-LAF14 and mt-LAF19 in other organisms, mt-LAF4 shares structural homology with the bacterial tRNA pseudouridine synthase TruD and the eukaryotic pseudouridine synthase Pus7. Although its overall catalytic domain fold shows structural homology (Figure S6F), the putative active site lacks the catalytic aspartate and the positively charged rRNA binding cleft found in TruD. Therefore, the pseudouridine synthase fold of mt-LAF4 is presumably used by this assembly factor to specifically recognize the immature fold of this functionally important rRNA region.

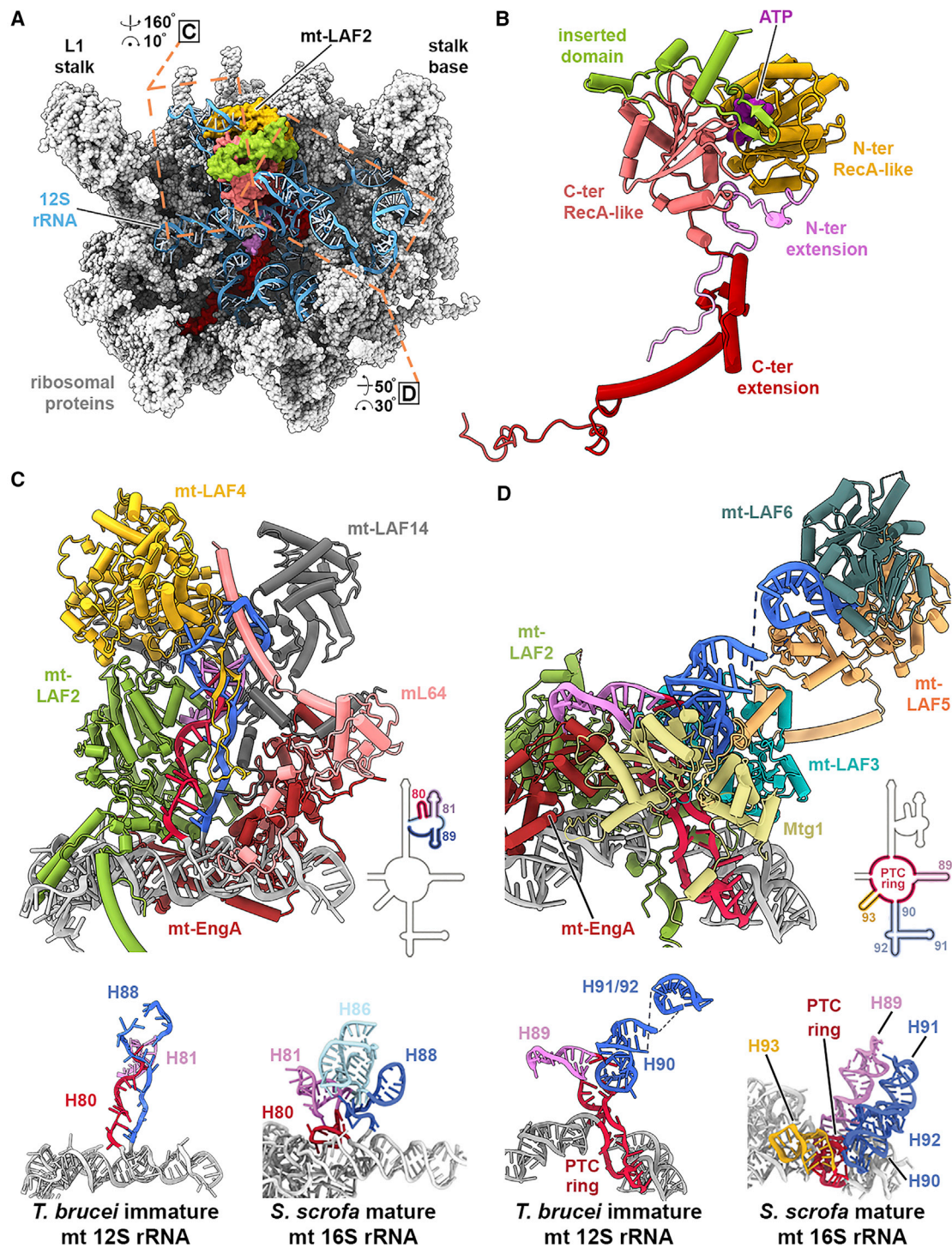


Figure 4. Assembly Factors Involved in the PTC Maturation

(A) State B of the mitoribosomal LSU assembly intermediate is shown from the intersubunit side, with the mitoribosomal proteins in gray and the 12S rRNA in blue. Assembly factor mt-LAF2 is shown in a surface view, with its domains in different colors. Other assembly factors are hidden (see also Figure S5).

(B) The assembly factor mt-LAF2 is illustrated, with its domains labeled and color-coded as in (A).

(C and D) Immature fold (H80–88) (C) and H89–92 (D) of the 12S rRNA are shown, with surrounding assembly factors colored individually. The immature fold of the rRNA regions is shown below, with a mature conformation of a corresponding fragment from *Sus scrofa* mitoribosomal 16S rRNA for comparison. rRNA fragments are colored as shown on the corresponding secondary structure diagrams of the 12S rRNA domain V.

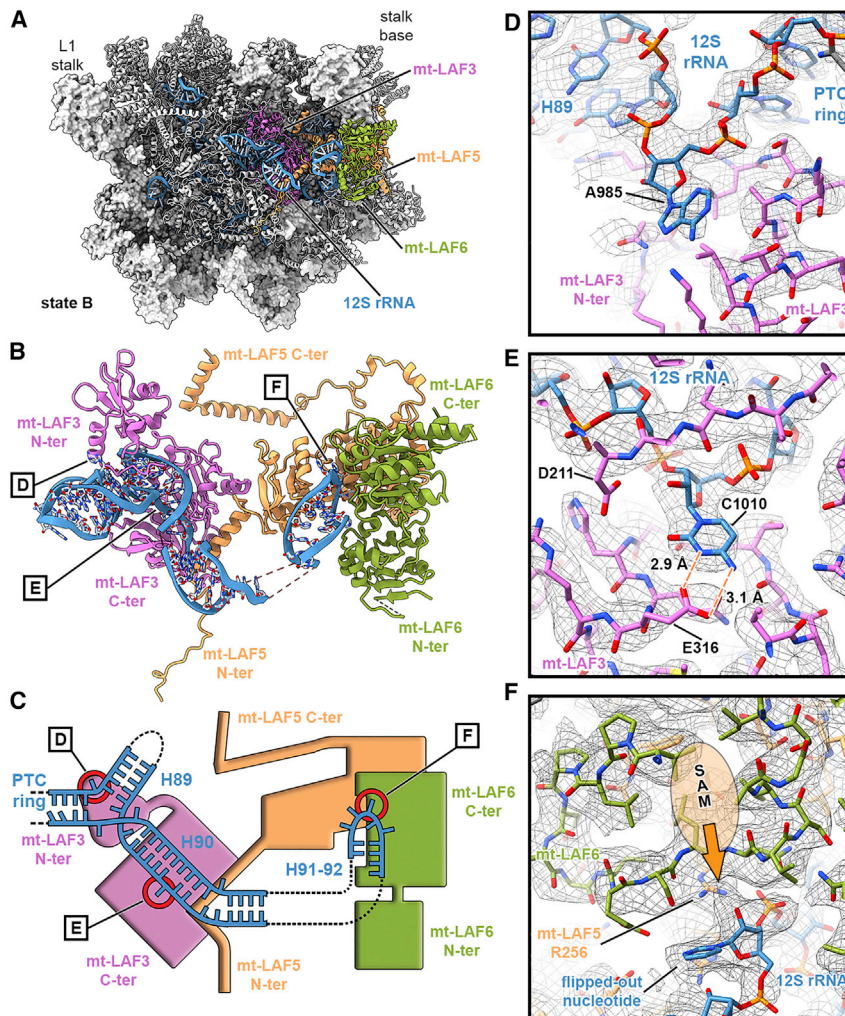


Figure 5. The Methyltransferase Heterodimer mt-LAF5/mt-LAF6 Binds the rRNA Helix 92

(A) View of the mitochondrial LSU assembly intermediate state B from the intersubunit side. The mitochondrial proteins and assembly factors, colored gray, are represented as surfaces and illustrations, respectively, with the exception of mt-LAF3 (pink), mt-LAF5 (orange), and mt-LAF6 (green). The 12S rRNA is shown in blue.

(B and C) Interaction network between assembly factors mt-LAF3, mt-LAF5, and mt-LAF6 and the 12S rRNA elements that in the mature state form the PTC ring. H89–92 in the mature mitochondrial LSU are shown as ribbons (B) and as a schematic (C).

(D–F) The regions of the close-up views shown in (D)–(F) are indicated, with the nucleotides in focus circled in red. (D) The N-terminal domain of the pseudouridine synthase mt-LAF3 stabilizes the kink formed by 12S rRNA elements of the PTC ring and H89, while the C-terminal domain (E) harbors a cytosine nucleotide in its putative active site. (F) The nucleotides of the H91–92 region are sandwiched between the C-terminal domains of mt-LAF5 and mt-LAF6. The putative binding site of the cofactor SAM is indicated. In all 3 close ups, the uncarved cryo-EM density is shown as a black mesh.

alytic aspartic acid in mt-LAF3 (D211) and all of the other residues necessary for its enzymatic activity are conserved, trypanosomes carry a mutation in the vicinity of the binding pocket (L316E). This glutamic acid residue points toward the active site and forms hydrogen bonds with the bound cytosine. This interaction stabilizes the binding of the cytosine and tilts the nucleotide away from the catalytic residues

The other 12S rRNA elements of the PTC, in particular, the peptidyltransferase ring and the outgoing helices H89 to H92, are kept in an immature conformation by six assembly factors (Figures 4D and 5A). The peptidyltransferase ring and helices H89 and H90 in immature conformation create a three-way junction that is stabilized by mt-LAF3, a structural homolog of the bacterial RluA and mitochondrial RNA pseudouridine synthase RPUSD4 (Antonicka et al., 2017; Hoang et al., 2006; Zaganelli et al., 2017). mt-LAF3 comprises two domains acting as a clamp (Figures 5B and 5C). The N-terminal domain, lacking any close structural homology, interacts specifically with the three-way junction (Figure 5D). The C-terminal domain, structurally similar to the pseudouridine synthase, is sandwiched between the peptidyltransferase ring and H90. The specific interactions of mt-LAF3 with H90 introduce a kink in the canonical stem by flipping out an rRNA base into its active site, which prevents the formation of the standard helical structure (Figure 5E). Contrary to expectations, the flipped-out base is a cytosine (C1010) instead of a uridine, although the observed rRNA fold is related to the crystal structure of the RNA fragment bound to bacterial pseudouridine synthase RluA (Hoang et al., 2006) (Figure S6E). Although the cat-

(Figure 5E). Our observations suggest that mt-LAF3 plays an rRNA scaffolding role rather than a catalytic role during the visualized mitochondrial LSU assembly states. However, RNAi-mediated gene knockdown of mt-LAF3, apart from slowing down the growth of *T. brucei* cells, not only reduces the steady-state levels of the 12S rRNA by 60% after 72-h post-induction but also affects the stability of the 9S rRNA to a similar extent (Figure 2E). This suggests that mt-LAF3 plays an additional role in SSU maturation or in rRNA post-transcriptional processing.

The presented results indicate that, although many regions of the LSU are already in a mature conformation, the PTC region of the rRNA is still immature and interacts with numerous assembly factors. The PTC is also one of the last regions of the LSU to mature in prokaryotic and eukaryotic cytoplasmic ribosomes (Baßler and Hurt, 2019; Davis and Williamson, 2017).

A Methyltransferase Binds to a Conserved Site of rRNA Modification in the A-Loop

In a translating ribosome, H92 (A-loop) interacts with the cytosine-cytosine-adenine (CCA) end of the A-site tRNA and is crucial for the LSU activity. In both assembly intermediates,

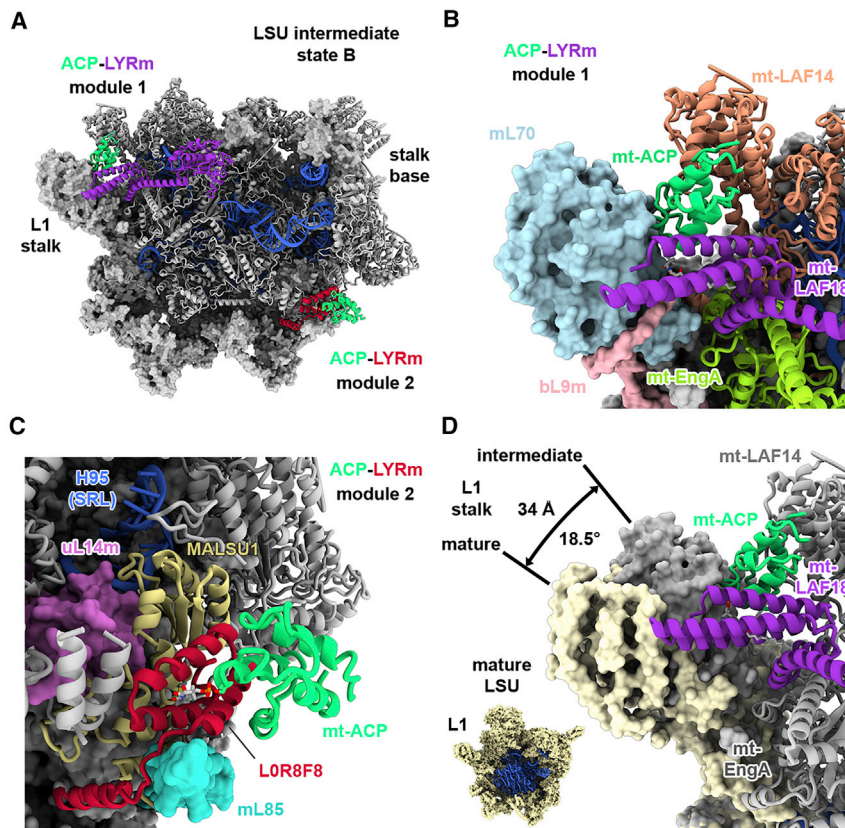


Figure 6. The ACP-LYRm Modules in the LSU Assembly Intermediates

(A) An overview of the state B assembly intermediate is shown from the intersubunit side. The ribosomal proteins are represented as surfaces and the assembly factors as illustrations.

(B and C) The ACP-LYRm modules 1 (B) and 2 (C) are presented as close-up views.

(D) Models of state B (gray) and of the mature LSU (yellow) are overlaid to indicate the conformational shift of the L1 stalk by 34 Å (18.5°) induced by the ACP-LYRm module 1. In the inset, the mature LSU with proteins in yellow and the 12S rRNA in blue are shown for orientation. See also Figure S4D.

helices 90–92 are protruding from the 3-way junction and are positioned in a cleft shaped by mt-LAF5 and mt-LAF6 (Figure 5C). Both assembly factors belong to the SpoUT methyltransferases (MTase) superfamily (Anantharaman et al., 2002) and form a heterodimer. mt-LAF6 harbors a conserved set of S-adenosylmethionine (SAM)-binding residues, while mt-LAF5 represents an inactive variant due to the mutations in cofactor-binding residues and resulting rearrangement in the binding pocket. Although enzymatically inactive, mt-LAF5 is likely important for the activity of mt-LAF6 since it contributes in *trans* a critical active site residue (Figure 5F), similar to that described for the homodimeric methyltransferase NshR that methylates the bacterial 23S rRNA of *Streptomyces actuosus* (Yang et al., 2010). In addition, mt-LAF5 acts as a docking site, anchoring mt-LAF6 to the LSU assembly intermediate via long N- and C-terminal extensions that interact with multiple other assembly factors and mitochondrial proteins. mt-LAF6 faces its catalytic cleft toward the rRNA hairpin loop formed by H92, the nucleotides of which are methylated in the mitochondria of different eukaryotic species (Pintard et al., 2002; Rorbach et al., 2014). Although we could not establish the identity of individual nucleotides in H92 due to lower local resolution of the rRNA in that region, we observed a flipped-out nucleotide that points toward the active site of mt-LAF6 (Figure 5F). In both states, no SAM cofactor is observed in the active site of mt-LAF6; however, the position of the flipped-out nucleotide suggests that mt-LAF6 is an active methyltrans-

ferase involved in 2'-O-ribose methylation of a nucleotide in the H92 loop and therefore may function analogously to MRM2 or MRM3, the 2'-O-MTases that modify Um1369 and Gm1370, respectively, in the A-loop of human mitochondria (Rorbach et al., 2014).

A Novel ACP-LYRm Module Binds and Changes the Conformation of the L1 Stalk

In mitochondria, the ACP to which a 4'-phosphopantetheine group is covalently attached plays a critical role in the biosynthesis pathway of fatty and lipionic acids by

shuttling the growing acyl chain from one enzyme to the other (Cronan et al., 2005). The ACP has also been observed as a component of mitochondrial multisubunit complexes, such as the nicotinamide adenine dinucleotide + hydrogen (NADH):ubiquinone oxidoreductase (complex 1) (Fiedorczuk et al., 2016; Zhu et al., 2016) or the iron-sulfur cluster (ISC) assembly machinery (Boniecki et al., 2017). In addition, recent structural studies found ACP attached to assembly intermediates of both the human mitoribosomal LSU (Brown et al., 2017) and the trypanosomal mitoribosomal SSU (Saurer et al., 2019). In all of these complexes, the ACPs and their covalently linked acyl-phosphopantetheine moieties specifically interact with proteins that contain a LYR-motif (LYRm) characterized by consecutive leucine, tyrosine, and arginine residues (Figures 6 and S4D).

We found two such ACP-LYRm modules as architectural components of the trypanosomal LSU assembly intermediates (Figure 6A). Module 1, in which mt-LAF18 contributes the LYRm is present in both states and located near the L1 stalk (Figure 6B). Besides the interaction with mt-LAF18, the ACP acts as a bridge between mt-LAF14 and ribosomal proteins mL70 and mL74 of the L1 stalk, causing a tilt of the L1 stalk by 34 Å (18.5°) toward the CP region of the subunit in comparison to the conformation in the mature LSU (Figure 6D). Module 2 is observed only in state B near the SRL (H95), where it replaces state A-specific factors. There, the ACP binds the LYRm containing protein LOR8F8, which in turn interacts with mitochondrial assembly factor MALSU1, forming the MALSU1-LOR8F8-ACP complex (Figures

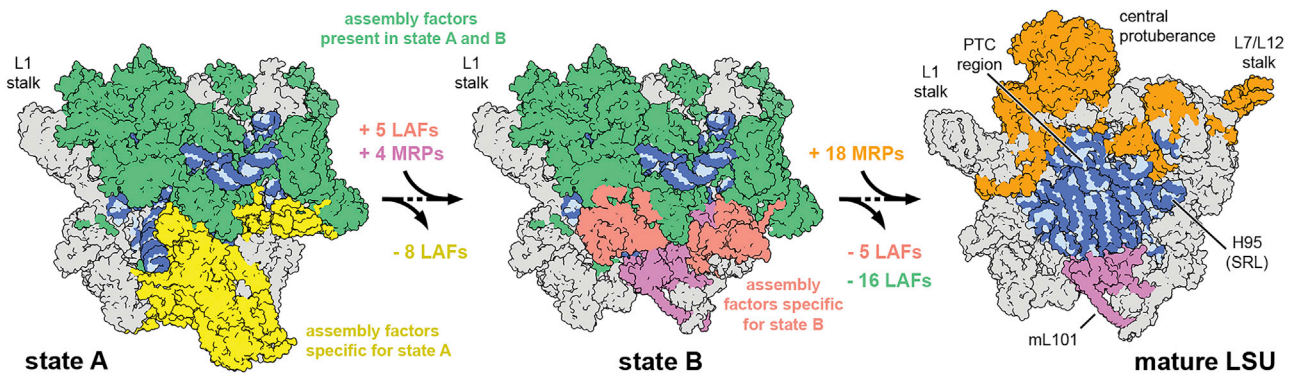


Figure 7. The Assembly Process of the *T. brucei* Mitochondrial LSU

The structures of the mitoribosomal LSU assembly intermediates states A and B and of the mature LSU, including a modeled 12S rRNA, are represented as surfaces from the intersubunit side. They are ordered in the most likely sequence of assembly, based on their structural features. Assembly factors are colored green (states A and B), yellow (specific for state A), and red (specific for state B). Mitoribosomal proteins are colored gray (states A and B and mature LSU), violet (in state B and mature LSU), and orange (mature LSU). The 12S rRNA is colored in blue. Landmarks of the LSU and selected elements are labeled.

6C and S6D) that was previously observed bound to the late-state intermediate of the human mitoribosomal LSU (Brown et al., 2017). As in the human LSU assembly intermediates, this complex interacts with uL14m that joins the *T. brucei* LSU upon progression to state B. Brown and colleagues suggested that the MALSU1-LOR8F8-ACP module prevents the association of the mitoribosomal SSU to the immature LSU through steric clashes. Both ACP-LYRm modules found in the *T. brucei* assembly intermediates would accomplish the suggested function.

DISCUSSION

Although bacterial and eukaryotic cytosolic ribosome maturation has been extensively studied (Baßler and Hurt, 2019; Davis and Williamson, 2017), the assembly of mitoribosomes is relatively poorly understood. However, advances in EM and the recent breakthroughs in determining the atomic structures of mature mitoribosomes (Amunts et al., 2015; Desai et al., 2017; Greber et al., 2015) permit structural and mechanistic investigations of the mitoribosome biogenesis in different organisms.

Here, we present the atomic cryo-EM structures of two mitoribosomal LSU assembly intermediates, referred to as state A and state B (Figure 1) that were prepared from wild-type *T. brucei* cells. In both states, the ribosomal proteins and the 12S rRNA elements located on the solvent-accessible side, which does not contact the SSU, are in their mature state. However, the 12S rRNA elements that form the key functional elements, such as the tRNA binding sites, the PTC, and the upper part of the polypeptide exit tunnel, are held in immature conformations stabilized by an extensive protein network formed by multiple assembly factors. The observed states agree with the assembly sequence observed for the mammalian mitoribosomal LSU, in which the PTC folds last (Brown et al., 2017). It appears that protein-rich mitoribosomes follow the established order of eukaryotic large ribosomal subunit assembly (Konikkat and Woolford, 2017), in which the ribosomal protein shell forms early during the maturation process and assembles almost independently of the rRNA core.

The structures provide additional evidence that the assembly of mitoribosomes occurs through the hierarchical assembly of preformed clusters of proteins (Figure 7), as previously suggested by biochemical experiments (Bogenhagen et al., 2018; Zeng et al., 2018). During the transition from intermediate state A to B, at least nine assembly factors forming two separate clusters at the lower intersubunit side of state A are replaced by four mitoribosomal proteins and five new assembly factors. The modular exchange is accompanied by conformational changes in the 12S rRNA and mitoribosomal protein elements. During the transition from assembly intermediate state B to the mature LSU, which probably includes multiple steps and intermediates, all of the remaining assembly factors must leave such that the 12S rRNA core, including the PTC, can adopt its mature fold. These observations suggest that even the previously described mitoribosomal LSU (Ramrath et al., 2018) may represent a very late assembly intermediate with still-unstructured PTC and possibly some assembly factors still bound to the exit region of the large ribosomal subunit as described for the *Leishmania tarentolae* mitoribosome (Soufari et al., 2020). Multiple mitoribosomal proteins must join state B to form the missing parts of the LSU, in particular, the CP and elements of the L1 and the L7/L12 stalks. Considering that in the *T. brucei* mitoribosome the CP is composed entirely of ribosomal proteins, it is likely that it joins as a preassembled complex. In fact, classification of our particle datasets revealed further states of assembly intermediates that probably occur between state B and the mature LSU, but could not be resolved to high resolution (Figure S1). However, their structural features support the idea that the CP joins as a module and incorporates stepwise through distinct conformational states until it adopts its mature position. Likewise, it was proposed that CP components associate as a module during the assembly of yeast mitoribosomes (Zeng et al., 2018).

Our structures agree well with the proposed assembly order of the yeast 54S subunit (Zeng et al., 2018) and probably correspond to an intermediate stage (p₂54S) in the yeast maturation pathway (Figure S7C). Nevertheless, there are few exceptions, possibly due to the different protein compositions and

architectures of trypanosomal mitoribosomes. The similarities to the order of events proposed for the mammalian 39S subunit assembly pathway are less obvious (Figure S7D) (Bogenhagen et al., 2018). In particular, the proteins forming the CP are incorporated at early stages of mammalian 39S maturation, in contrast to the observations for the yeast and trypanosomal LSU maturation. Although mitoribosomes diverged considerably from bacterial ribosomes, the set of ribosomal proteins still missing in the trypanosomal mitoribosomal LSU intermediates matches the ones missing in the late-state intermediates of the bacterial LSU (Figure S7B) (Jomaa et al., 2014; Li et al., 2013; Nikolay et al., 2018).

The assembly of trypanosomal mitoribosomes is assisted by numerous assembly factors, with 25 LAFs present in state A and 19 LAFs present in state B. Comparisons based on sequence and structural features revealed that many of the observed LAFs are homologous to the ribosomal assembly factors previously described in bacteria or in mitochondria (Figure S6). In particular, the module formed by MALSU1, LOR8F8, and mt-ACP was found in late-state intermediates of the human 39S subunit (Brown et al., 2017), indicating that the observations described here may be applicable in understanding mitoribosomal assembly pathways in other organisms. Furthermore, some factors that were known to participate in mitoribosome biogenesis, such as Mtg1 and mt-EngA-GTP₂ (Gupta et al., 2018; Kim and Barrientos, 2018; Kotani et al., 2013), are described here for the first time in complex with the immature mitoribosome, helping us to understand their molecular function. The GTPases EngA-GTP₂, EngB-GTP, and Mtg1 probably play an active role in the assembly process by inducing conformational changes within the assembly that control the release and binding of assembly factors and mitoribosomal proteins. Since they interact with such an extensive region of the intersubunit side, they may also sense a particular conformation of the 12S rRNA. Therefore, it is plausible that the observed intermediates correspond to some of the rate-limiting steps during assembly that are resolved only when a certain conformation of the 12S rRNA leads to GTP hydrolysis and dissociation of the GTPases. Furthermore, the GTPases may link mitoribosome biogenesis to the mitochondrial GTP:GDP ratio, similar to that proposed for the GTPases involved in cytoplasmic ribosome assembly, linking ribosomal maturation to the cellular energy level (Britton, 2009). Other assembly factors that show structural homology to enzymes, such as mt-LAF4 homologous to the tRNA pseudouridine synthase TruD, have lost their enzymatic activity. They probably act as a scaffold or specifically recognize important elements of the 12S rRNA, thereby promoting their correct folding. Structural homologs and functional analogs of the newly identified assembly factors may also play a role in mitoribosome maturation in other eukaryotes, including humans.

In conclusion, the presented structures of two late-stage assembly intermediates of the *T. brucei* mitoribosomal LSU provide a wealth of information that advances our understanding of ribosomal biogenesis. The numerous identified assembly factors provide an excellent starting point for future biochemical and functional studies of mitoribosomal maturation in trypanosomes and other eukaryotes, including humans. Furthermore, the created RNAi knockdown strains present an interesting sys-

tem for further structural analysis of other mitochondrial LSU assembly intermediates. Considering that trypanosomes are parasites causing severe diseases in humans and domestic animals and that mitochondrial translation is essential for the disease-causing bloodstream form of trypanosomes, components of the discovered assembly pathway may serve as possible drug targets for treatment against such diseases (Niemann et al., 2011).

STAR★METHODS

Detailed methods are provided in the online version of this paper and include the following:

- KEY RESOURCES TABLE
- RESOURCE AVAILABILITY
 - Lead Contact
 - Materials Availability
 - Data and Code Availability
- EXPERIMENTAL MODEL AND SUBJECT DETAILS
 - Trypanosoma brucei strains
- METHOD DETAILS
 - Transgenic cell lines
 - Growth curves
 - Preparation of mitochondrial vesicles
 - Native *T. brucei* mitoribosome purification
 - Cryo-EM sample preparation and data acquisition
 - Cryo-EM data processing of the mitoribosomal sample
 - Model building and refinement
 - Northern Analysis for mitochondrial rRNAs
- QUANTIFICATION AND STATISTICAL ANALYSIS
 - Creation of Figures

SUPPLEMENTAL INFORMATION

Supplemental Information can be found online at <https://doi.org/10.1016/j.molcel.2020.06.030>.

ACKNOWLEDGMENTS

We thank Martin Saurer and Ahmad Jomaa for critically reading the manuscript and for helpful discussions. We also thank Mauro Fischli for help at the early stage of the biochemical work and Bernd Schimanski for the BS19.3 single marker cell line. The cryo-EM data were collected at the Scientific Center for Optical and Electron Microscopy (ScopeM) at ETH Zurich, and we thank P. Tittmann and M. Peterek for their support. The cryo-EM data were processed on the Leonhard computing cluster of the Swiss National Supercomputing Centre (CSCS). This work was supported by the Swiss National Science Foundation (SNSF) grant 310030B_163478 and the National Center of Excellence in Research (NCCR) RNA & Disease program of the SNSF grant 138262, Ernst Jung Prize, Otto Naegeli Prize, as well as by ETH Research Grant ETH-40 16-2 to N.B. D.J.F.R. was supported by a Federation of European Biochemical Societies (FEBS) long-term fellowship. S.M. was supported by a European Molecular Biology Organization (EMBO) long-term fellowship (ALTF 793-2017) and a Human Frontier Science Program long-term fellowship (LT000008/2018-L).

AUTHOR CONTRIBUTIONS

M.N., D.J.F.R., S.C., and E.K.H. prepared the *T. brucei* cell cultures and purified the mitochondrial vesicles. M.N. and S.C. prepared the transgenic *T. brucei* cell lines and performed the RNAi experiments. M.N., S.C., and

A.S. designed and analyzed the *T. brucei* experiments. D.J.F.R. and S.M. purified the *T. brucei* mitochondrial particles and prepared the cryo-EM grids. D.J.F.R., S.M., and D.B. collected the cryo-EM data of the mitochondrial sample. D.J.F.R., S.M., and M.J. calculated the cryo-EM density maps. D.J.F.R. and P.B. built the initial atomic models. M.L. and M.J. refined and validated the final molecular models. M.J., P.B., D.J.F.R., M.L., and N.B. interpreted the structures. P.B., M.J., M.N., and S.C. created the figures. M.J., P.B., and N.B. wrote the manuscript. All of the authors contributed to the final version of the manuscript.

DECLARATION OF INTERESTS

The authors declare no competing interests.

Received: February 27, 2020

Revised: May 4, 2020

Accepted: June 11, 2020

Published: July 16, 2020

REFERENCES

- Adams, P.D., Afonine, P.V., Bunkóczi, G., Chen, V.B., Davis, I.W., Echols, N., Headd, J.J., Hung, L.-W., Kapral, G.J., Grosse-Kunstleve, R.W., et al. (2010). PHENIX: a comprehensive Python-based system for macromolecular structure solution. *Acta Crystallogr. D Biol. Crystallogr.* **66**, 213–221.
- Afonine, P.V., Poon, B.K., Read, R.J., Sobolev, O.V., Terwilliger, T.C., Urzhumtsev, A., and Adams, P.D. (2018). Real-space refinement in PHENIX for cryo-EM and crystallography. *Acta Crystallogr D Struct Biol.* **74**, 531–544, <https://doi.org/10.1107/S2059798318006551>.
- Altschul, S.F., Gish, W., Miller, W., Myers, E.W., and Lipman, D.J. (1990). Basic local alignment search tool. *J. Mol. Biol.* **215**, 403–410.
- Amunts, A., Brown, A., Toots, J., Scheres, S.H.W., and Ramakrishnan, V. (2015). Ribosome. The structure of the human mitochondrial ribosome. *Science* **348**, 95–98.
- Anantharaman, V., Koonin, E.V., and Aravind, L. (2002). SPOUT: a class of methyltransferases that includes spoU and trmD RNA methylase superfamilies, and novel superfamilies of predicted prokaryotic RNA methylases. *J. Mol. Microbiol. Biotechnol.* **4**, 71–75.
- Ansmant, I., Massenet, S., Grosjean, H., Motorin, Y., and Branlant, C. (2000). Identification of the *Saccharomyces cerevisiae* RNA:pseudouridine synthase responsible for formation of psi(2819) in 21S mitochondrial ribosomal RNA. *Nucleic Acids Res.* **28**, 1941–1946.
- Antonicka, H., Choquet, K., Lin, Z.Y., Gingras, A.C., Kleinman, C.L., and Shoubridge, E.A. (2017). A pseudouridine synthase module is essential for mitochondrial protein synthesis and cell viability. *EMBO Rep.* **18**, 28–38.
- Aslett, M., Aurrecochea, C., Berriman, M., Brestelli, J., Brunk, B.P., Carrington, M., Depledge, D.P., Fischer, S., Gajria, B., Gao, X., et al. (2010). TriTrypDB: a functional genomic resource for the Trypanosomatidae. *Nucleic Acids Res.* **38**, D457–D462.
- Barrientos, A., Korr, D., Barwell, K.J., Sjulsen, C., Gajewski, C.D., Manfredi, G., Ackerman, S., and Tzagoloff, A. (2003). MTG1 codes for a conserved protein required for mitochondrial translation. *Mol. Biol. Cell* **14**, 2292–2302.
- Baßler, J., and Hurt, E. (2019). Eukaryotic Ribosome Assembly. *Annu. Rev. Biochem.* **88**, 281–306.
- Bharat, A., Jiang, M., Sullivan, S.M., Maddock, J.R., and Brown, E.D. (2006). Cooperative and critical roles for both G domains in the GTPase activity and cellular function of ribosome-associated *Escherichia coli* EngA. *J. Bacteriol.* **188**, 7992–7996.
- Bogenhagen, D.F., Ostermeyer-Fay, A.G., Haley, J.D., and Garcia-Diaz, M. (2018). Kinetics and Mechanism of Mammalian Mitochondrial Ribosome Assembly. *Cell Rep.* **22**, 1935–1944.
- Boniecki, M.T., Freibert, S.A., Mühlhoff, U., Lill, R., and Cygler, M. (2017). Structure and functional dynamics of the mitochondrial Fe/S cluster synthesis complex. *Nat. Commun.* **8**, 1287.
- Britton, R.A. (2009). Role of GTPases in bacterial ribosome assembly. *Annu. Rev. Microbiol.* **63**, 155–176.
- Brown, A., Rathore, S., Kimanius, D., Aibara, S., Bai, X.C., Rorbach, J., Amunts, A., and Ramakrishnan, V. (2017). Structures of the human mitochondrial ribosome in native states of assembly. *Nat. Struct. Mol. Biol.* **24**, 866–869.
- Brun, R., and Schönenberger. (1979). Cultivation and in vitro cloning or procyclic culture forms of *Trypanosoma brucei* in a semi-defined medium. Short communication. *Acta Trop.* **36**, 289–292.
- Chen, S.S., and Williamson, J.R. (2013). Characterization of the ribosome biogenesis landscape in *E. coli* using quantitative mass spectrometry. *J. Mol. Biol.* **425**, 767–779.
- Chomczynski, P., and Sacchi, N. (1987). Single-Step Method of RNA Isolation by Acid Guanidinium Thiocyanate–Phenol–Chloroform Extraction. *Anal Biochem* **162**, 156–159, <https://doi.org/10.1006/abio.1987.9999>.
- Cronan, J.E., Fearnley, I.M., and Walker, J.E. (2005). Mammalian mitochondria contain a soluble acyl carrier protein. *FEBS Lett.* **579**, 4892–4896.
- Cross, G.A. (1975). Identification, purification and properties of clone-specific glycoprotein antigens constituting the surface coat of *Trypanosoma brucei*. *Parasitology* **71**, 393–417.
- Davis, J.H., and Williamson, J.R. (2017). Structure and dynamics of bacterial ribosome biogenesis. *Philos. Trans. R. Soc. Lond. Ser. B Biol. Sci.* **372**, 20160181.
- Davis, J.H., Tan, Y.Z., Carragher, B., Potter, C.S., Lyumkis, D., and Williamson, J.R. (2016). Modular Assembly of the Bacterial Large Ribosomal Subunit. *Cell* **167**, 1610–1622.e15.
- de la Cruz, J., Karbstein, K., and Woolford, J.L., Jr. (2015). Functions of ribosomal proteins in assembly of eukaryotic ribosomes in vivo. *Annu. Rev. Biochem.* **84**, 93–129.
- De Silva, D., Tu, Y.-T., Amunts, A., Fontanesi, F., and Barrientos, A. (2015). Mitochondrial ribosome assembly in health and disease. *Cell Cycle* **14**, 2226–2250.
- De Silva, D., Poliquin, S., Zeng, R., Zamudio-Ochoa, A., Marrero, N., Perez-Martinez, X., Fontanesi, F., and Barrientos, A. (2017). The DEAD-box helicase Mss116 plays distinct roles in mitochondrial ribogenesis and mRNA-specific translation. *Nucleic Acids Res.* **45**, 6628–6643.
- Del Campo, M., and Lambowitz, A.M. (2009). Structure of the Yeast DEAD box protein Mss116p reveals two wedges that crimp RNA. *Mol. Cell* **35**, 598–609.
- Desai, N., Brown, A., Amunts, A., and Ramakrishnan, V. (2017). The structure of the yeast mitochondrial ribosome. *Science* **355**, 528–531.
- Emsley, P., Lohkamp, B., Scott, W.G., and Cowtan, K. (2010). Features and development of Coot. *Acta Crystallogr. D Biol. Crystallogr.* **66**, 486–501.
- Fairman-Williams, M.E., Guenther, U.-P., and Jankowsky, E. (2010). SF1 and SF2 helicases: family matters. *Curr. Opin. Struct. Biol.* **20**, 313–324.
- Fiedorczuk, K., Letts, J.A., Degliesposti, G., Kaszuba, K., Skehel, M., and Sazanov, L.A. (2016). Atomic structure of the entire mammalian mitochondrial complex I. *Nature* **538**, 406–410.
- Goddard, T.D., Huang, C.C., Meng, E.C., Pettersen, E.F., Couch, G.S., Morris, J.H., and Ferrin, T.E. (2018). UCSF ChimeraX: meeting modern challenges in visualization and analysis. *Protein Sci.* **27**, 14–25.
- Greber, B.J., Bieri, P., Leibundgut, M., Leitner, A., Aebersold, R., Boehringer, D., and Ban, N. (2015). Ribosome. The complete structure of the 55S mammalian mitochondrial ribosome. *Science* **348**, 303–308.
- Gulati, M., Jain, N., Anand, B., Prakash, B., and Britton, R.A. (2013). Mutational analysis of the ribosome assembly GTPase RbgA provides insight into ribosome interaction and ribosome-stimulated GTPase activation. *Nucleic Acids Res.* **41**, 3217–3227.

- Gupta, K., Gupta, A., Haider, A., and Habib, S. (2018). Characterization of mitochondrial-targeted GTPases in *Plasmodium falciparum*. *Parasitology* *145*, 1600–1612.
- Hillman, G.A., and Henry, M.F. (2019). The yeast protein Mam33 functions in the assembly of the mitochondrial ribosome. *J. Biol. Chem.* *294*, 9813–9829, <https://doi.org/10.1074/jbc.RA119.008476>.
- Hoang, C., Chen, J., Vizthum, C.A., Kandel, J.M., Hamilton, C.S., Mueller, E.G., and Ferré-D'Amaré, A.R. (2006). Crystal structure of pseudouridine synthase RluA: indirect sequence readout through protein-induced RNA structure. *Mol. Cell* *24*, 535–545.
- Hwang, J., and Inouye, M. (2006). The tandem GTPase, Der, is essential for the biogenesis of 50S ribosomal subunits in *Escherichia coli*. *Mol. Microbiol.* *61*, 1660–1672.
- Jomaa, A., Jain, N., Davis, J.H., Williamson, J.R., Britton, R.A., and Ortega, J. (2014). Functional domains of the 50S subunit mature late in the assembly process. *Nucleic Acids Res.* *42*, 3419–3435.
- Kelley, L.A., Mezulis, S., Yates, C.M., Wass, M.N., and Sternberg, M.J. (2015). The Phyre2 web portal for protein modeling, prediction and analysis. *Nat. Protoc.* *10*, 845–858.
- Kim, H.J., and Barrientos, A. (2018). MTG1 couples mitoribosome large subunit assembly with intersubunit bridge formation. *Nucleic Acids Res.* *46*, 8435–8453.
- Kim, H.J., Maiti, P., and Barrientos, A. (2017). Mitochondrial ribosomes in cancer. *Semin. Cancer Biol.* *47*, 67–81.
- Klinge, S., and Woolford, J.L., Jr. (2019). Ribosome assembly coming into focus. *Nat. Rev. Mol. Cell Biol.* *20*, 116–131.
- Konikkat, S., and Woolford, J.L., Jr. (2017). Principles of 60S ribosomal subunit assembly emerging from recent studies in yeast. *Biochem. J.* *474*, 195–214.
- Kotani, T., Akabane, S., Takeyasu, K., Ueda, T., and Takeuchi, N. (2013). Human G-proteins, ObgH1 and Mtg1, associate with the large mitochondrial ribosome subunit and are involved in translation and assembly of respiratory complexes. *Nucleic Acids Res.* *41*, 3713–3722.
- Li, N., Chen, Y., Guo, Q., Zhang, Y., Yuan, Y., Ma, C., Deng, H., Lei, J., and Gao, N. (2013). Cryo-EM structures of the late-stage assembly intermediates of the bacterial 50S ribosomal subunit. *Nucleic Acids Res.* *41*, 7073–7083.
- Matsuo, Y., Morimoto, T., Kuwano, M., Loh, P.C., Oshima, T., and Ogasawara, N. (2006). The GTP-binding protein YlqF participates in the late step of 50S ribosomal subunit assembly in *Bacillus subtilis*. *J. Biol. Chem.* *281*, 8110–8117.
- Mohr, G., Del Campo, M., Mohr, S., Yang, Q., Jia, H., Jankowsky, E., and Lambowitz, A.M. (2008). Function of the C-terminal domain of the DEAD-box protein Mss116p analyzed in vivo and in vitro. *J. Mol. Biol.* *375*, 1344–1364.
- Ni, X., Davis, J.H., Jain, N., Razi, A., Benlekbir, S., McArthur, A.G., Rubinstein, J.L., Britton, R.A., Williamson, J.R., and Ortega, J. (2016). YphC and YsxC GTPases assist the maturation of the central protuberance, GTPase associated region and functional core of the 50S ribosomal subunit. *Nucleic Acids Res.* *44*, 8442–8455.
- Niemann, M., and Schneider, A. (2020). A Scalable Purification Method for Mitochondria from *Trypanosoma brucei*. *Methods Mol. Biol.* *2116*, 611–626.
- Niemann, M., Schneider, A., and Cristodero, M. (2011). Mitochondrial translation in trypanosomatids: a novel target for chemotherapy? *Trends Parasitol.* *27*, 429–433.
- Nikolay, R., Hilal, T., Qin, B., Mielke, T., Bürger, J., Loerke, J., Textoris-Taube, K., Nierhaus, K.H., and Spahn, C.M.T. (2018). Structural Visualization of the Formation and Activation of the 50S Ribosomal Subunit during In Vitro Reconstitution. *Mol. Cell* *70*, 881–893.e3.
- Ott, M., Amunts, A., and Brown, A. (2016). Organization and Regulation of Mitochondrial Protein Synthesis. *Annu. Rev. Biochem.* *85*, 77–101.
- Pintard, L., Bujnicki, J.M., Lapeyre, B., and Bonnerot, C. (2002). MRM2 encodes a novel yeast mitochondrial 21S rRNA methyltransferase. *EMBO J.* *21*, 1139–1147.
- Purta, E., O'Connor, M., Bujnicki, J.M., and Douthwaite, S. (2008). YccW is the m5C methyltransferase specific for 23S rRNA nucleotide 1962. *J. Mol. Biol.* *383*, 641–651.
- Putnam, A.A., and Jankowsky, E. (2013). DEAD-box helicases as integrators of RNA, nucleotide and protein binding. *Biochim. Biophys. Acta* *1829*, 884–893.
- Ramrath, D.J., Niemann, M., Leibundgut, M., Bieri, P., Prange, C., Horn, E.K., Leitner, A., Boehringer, D., Schneider, A., and Ban, N. (2018). Evolutionary shift toward protein-based architecture in trypanosomal mitochondrial ribosomes. *Science* *362*, eaau7735.
- Roger, A.J., Muñoz-Gómez, S.A., and Kamikawa, R. (2017). The Origin and Diversification of Mitochondria. *Curr. Biol.* *27*, R1177–R1192.
- Rorbach, J., Boesch, P., Gammage, P.A., Nicholls, T.J., Pearce, S.F., Patel, D., Hauser, A., Perocchi, F., and Minczuk, M. (2014). MRM2 and MRM3 are involved in biogenesis of the large subunit of the mitochondrial ribosome. *Mol. Biol. Cell* *25*, 2542–2555.
- Ruzhenikov, S.N., Das, S.K., Sedelnikova, S.E., Baker, P.J., Artymiuk, P.J., Garcia-Lara, J., Foster, S.J., and Rice, D.W. (2004). Analysis of the open and closed conformations of the GTP-binding protein YsxC from *Bacillus subtilis*. *J. Mol. Biol.* *339*, 265–278.
- Saurer, M., Ramrath, D.J.F., Niemann, M., Calderaro, S., Prange, C., Mattei, S., Scaiola, A., Leitner, A., Bieri, P., Horn, E.K., et al. (2019). Mitoribosomal small subunit biogenesis in trypanosomes involves an extensive assembly machinery. *Science* *365*, 1144–1149.
- Schaefer, L., Uicker, W.C., Wicker-Planquart, C., Foucher, A.-E., Jault, J.-M., and Britton, R.A. (2006). Multiple GTPases participate in the assembly of the large ribosomal subunit in *Bacillus subtilis*. *J. Bacteriol.* *188*, 8252–8258.
- Seffouh, A., Jain, N., Jahagirdar, D., Basu, K., Razi, A., Ni, X., Guarné, A., Britton, R.A., and Ortega, J. (2019). Structural consequences of the interaction of RbgA with a 50S ribosomal subunit assembly intermediate. *Nucleic Acids Res.* *47*, 10414–10425.
- Sengoku, T., Nureki, O., Nakamura, A., Kobayashi, S., and Yokoyama, S. (2006). Structural basis for RNA unwinding by the DEAD-box protein *Drosophila* Vasa. *Cell* *125*, 287–300.
- Shajani, Z., Sykes, M.T., and Williamson, J.R. (2011). Assembly of bacterial ribosomes. *Annu. Rev. Biochem.* *80*, 501–526.
- Soufari, H., Waltz, F., Parrot, C., Durrieu, S., Bochler, A., Kuhn, L., Sissler, M., and Hashem, Y. (2020). Structure of the full kinetoplast mitoribosome and insight on its large subunit maturation. *bioRxiv*. <https://doi.org/10.1101/2020.05.02.073890>.
- Theissen, B., Karow, A.R., Köhler, J., Gubaev, A., and Klostermeier, D. (2008). Cooperative binding of ATP and RNA induces a closed conformation in a DEAD box RNA helicase. *Proc. Natl. Acad. Sci. USA* *105*, 548–553.
- Tomar, S.K., Dhimole, N., Chatterjee, M., and Prakash, B. (2009). Distinct GDP/GTP bound states of the tandem G-domains of EngA regulate ribosome binding. *Nucleic Acids Res.* *37*, 2359–2370.
- Uicker, W.C., Schaefer, L., and Britton, R.A. (2006). The essential GTPase RbgA (YlqF) is required for 50S ribosome assembly in *Bacillus subtilis*. *Mol. Microbiol.* *59*, 528–540.
- Waldman, A.S. (2004). *Genetic Recombination: Reviews and Protocols* (Humana Press), pp. 53–86.
- Wirtz, E., Leal, S., Ochatt, C., and Cross, G.A. (1999). A tightly regulated inducible expression system for conditional gene knock-outs and dominant-negative genetics in *Trypanosoma brucei*. *Mol. Biochem. Parasitol.* *99*, 89–101.
- Woolford, J.L., Jr., and Baserga, S.J. (2013). Ribosome biogenesis in the yeast *Saccharomyces cerevisiae*. *Genetics* *195*, 643–681.
- Yang, H., Wang, Z., Shen, Y., Wang, P., Jia, X., Zhao, L., Zhou, P., Gong, R., Li, Z., Yang, Y., et al. (2010). Crystal structure of the nosiheptide-

- resistance methyltransferase of *Streptomyces actuosus*. *Biochemistry* **49**, 6440–6450.
- Zaganelli, S., Rebelo-Guiomar, P., Maundrell, K., Rozanska, A., Pierredon, S., Powell, C.A., Jourdain, A.A., Hulo, N., Lightowers, R.N., Chrzanowska-Lightowers, Z.M., et al. (2017). The Pseudouridine Synthase RPUSD4 Is an Essential Component of Mitochondrial RNA Granules. *J. Biol. Chem.* **292**, 4519–4532.
- Zeng, R., Smith, E., and Barrientos, A. (2018). Yeast Mitochondrial Large Subunit Assembly Proceeds by Hierarchical Incorporation of Protein Clusters and Modules on the Inner Membrane. *Cell Metab.* **27**, 645–656.e7.
- Zhang, K. (2016). Gctf: Real-time CTF determination and correction. *J. Struct. Biol.* **193**, 1–12.
- Zhang, X., Yan, K., Zhang, Y., Li, N., Ma, C., Li, Z., Zhang, Y., Feng, B., Liu, J., Sun, Y., et al. (2014). Structural insights into the function of a unique tandem GTPase EngA in bacterial ribosome assembly. *Nucleic Acids Res.* **42**, 13430–13439.
- Zheng, S.Q., Palovcak, E., Armache, J.-P., Verba, K.A., Cheng, Y., and Agard, D.A. (2017). MotionCor2: anisotropic correction of beam-induced motion for improved cryo-electron microscopy. *Nat. Methods* **14**, 331–332.
- Zhu, J., Vinothkumar, K.R., and Hirst, J. (2016). Structure of mammalian respiratory complex I. *Nature* **536**, 354–358.
- Zivanov, J., Nakane, T., Forsberg, B.O., Kimanius, D., Hagen, W.J., Lindahl, E., and Scheres, S.H. (2018). New tools for automated high-resolution cryo-EM structure determination in RELION-3. *eLife* **7**, e42166.

STAR★METHODS

KEY RESOURCES TABLE

REAGENT or RESOURCE	SOURCE	IDENTIFIER
Chemicals, Peptides, and Recombinant Proteins		
Sorbitol	Sigma	85529
Nycodenz	Alere Technologies AS	1002424
DNase I from bovine pancreas	Roche	10104159001
IgG Sepharose 6 Fast Flow	GE Healthcare	17-0969-01
Deposited Data		
Cryo-EM density map of assembly intermediate of <i>T. brucei</i> mitoribosomal LSU state A	This study	EMDB: 10999
Cryo-EM density map of assembly intermediate of <i>T. brucei</i> mitoribosomal LSU state B	This study	EMDB: 11000
Atomic model of assembly intermediate of <i>T. brucei</i> mitoribosomal LSU state A	This study	PDB: 6YXX
Atomic model of assembly intermediate of <i>T. brucei</i> mitoribosomal LSU state B	This study	PDB: 6YXY
Experimental Models: Cell Lines		
BS19.3 for 427-based RNAi cell lines	Saurer et al., 2019	N/A
mt-LAF1 RNAi	This study	N/A
mt-LAF2 RNAi	This study	N/A
mt-LAF3 RNAi	This study	N/A
mt-LAF4 RNAi	This study	N/A
mt-LAF5 RNAi	This study	N/A
mt-LAF17 RNAi	This study	N/A
mt-LAF21 RNAi	This study	N/A
mt-LAF26 RNAi	This study	N/A
Experimental Models: Organisms/Strains		
<i>Trypanosoma brucei</i> Lister strain 427	Cross, 1975	RRID: SCR_004786
<i>Trypanosoma brucei</i> Lister strain 29-13	Wirtz et al., 1999	RRID: SCR_004786
Oligonucleotides		
For oligonucleotides used in this study see Table S2	Microsynth AG	N/A
Recombinant DNA		
N/A	N/A	N/A
Software and Algorithms		
EPU	Thermo Fisher Scientific	https://www.thermofisher.com/us/en/home/electron-microscopy/products/software-em-3d-vis/epu-software.html
MotionCor2	Zheng et al., 2017	https://msg.ucsf.edu/em/software/motioncor2.html
GCTF	Zhang, 2016	https://www.mrc-lmb.cam.ac.uk/kzhang/
Relion-3	Zivanov et al., 2018	https://www3.mrc-lmb.cam.ac.uk/relion/index.php/Main_Page
Phyre2	Kelley et al., 2015	http://www.sbg.bio.ic.ac.uk/phyre2/html/page.cgi?id=index
Coot 0.8.9.1	Emsley et al., 2010	https://www2.mrc-lmb.cam.ac.uk/Personal/pemsley/cool/
Phenix	Adams et al., 2010	https://www.phenix-online.org/
Other		
Carbon coated holey copper grids R 2/2	Quantifoil	N/A

RESOURCE AVAILABILITY

Lead Contact

Further information and requests for resources and reagents should be directed to and will be fulfilled by the Lead Contact, Nenad Ban (ban@mol.biol.ethz.ch)

Materials Availability

Cell lines generated in this study will be made available on request by the Lead Contact with a completed Materials Transfer Agreement (MTA).

Data and Code Availability

The cryo-EM reconstructions of the assembly intermediates of the trypanosomal mitochondrial LSU have been deposited in the Electron Microscopy Data Bank (EMDB) under ID codes EMDB: 10999 (state A) and EMDB: 11000 (state B). The corresponding atomic models have been deposited in the Protein Data Bank (PDB) under ID codes PDB: 6YXX (state A) and PDB: 6YXY (state B).

EXPERIMENTAL MODEL AND SUBJECT DETAILS

Trypanosoma brucei strains

Trypanosoma brucei cells were grown in suspension culture at 27°C in SDM-79 (Brun and Schönberger, 1979) supplemented with 7.5 mg/L Hemin and 5% (v/v) heat-inactivated fetal calf serum (FCS) for strain 427 (Cross, 1975) or 10% (v/v) FCS for strain 29-13, (Wirtz et al., 1999). Cells were maintained in disposable 50 mL culture flasks (25 cm²) with closed lids in a temperate incubator and diluted accordingly to keep the cells in the exponential growth phase (density ca. 2x 10⁵ to 6x 10⁷ cells/mL). For large scale preparations of mitochondrial vesicles (see below), cells were grown in 2L Erlenmeyer flasks to a density of up to 6x10⁷ cells/mL in a total volume of 1-1.5 L at 27°C and shaking at 120 rpm. The vesicle preparation for small to large scale is described in detail in Niemann and Schneider (2020).

METHOD DETAILS

Transgenic cell lines

RNAi-competent cell line based on *Trypanosoma brucei* strain 427 (Cross, 1975) was used to generate the mt-LAF knockdown cell lines (phleomycin single marker cells, gift from B. Schimanski, University of Bern), whereas strain 29-13 (Wirtz et al., 1999) was used for generating the cell lines targeting mS29/mS54 and uL15m with RNAi. All these constructs were based on a derivative of the stem-loop vector pLEW100 (Wirtz et al., 1999) using the following inserts for the RNAi construct: mt-LAF1 (Tb927.7.1640) ORF nt 521-991, mt-LAF2 (Tb927.11.12930) ORF nt 918-1324, mt-LAF3 (Tb927.9.3350) ORF nt 407-877, mt-LAF4 (Tb927.11.5990) ORF nt 759-1228, mt-LAF5 (Tb927.9.12850) ORF nt 242-710, mt-LAF17 (Tb927.11.16990) ORF nt 731-1157, mt-LAF21 (Tb927.7.3510) ORF nt 240-662, mt-LAF26/KRIPP3 (Tb927.1.1160) ORF nt 385-863. Transfection and selection of clones of the above-mentioned strains was done as described (Waldman, 2004).

Growth curves

T. brucei cells were inoculated to a density of 1x 10⁶ cells/mL. The culture was divided and one half was induced for RNAi with 1μg/mL tetracycline (tet). Cells were counted approximately every 24 hours and diluted to 1x 10⁶ cells/mL accordingly.

Preparation of mitochondrial vesicles

Trypanosoma brucei strain 427 (Cross, 1975) was used for preparation of mitochondrial vesicles and the detailed protocol is described in Niemann and Schneider (2020). Briefly, *T. brucei* cells (ca. 20 L, up to 1x 10¹² cells) were harvested by centrifugation (e.g., 7,100rpm/11,000 x g at 4°C for 10 min in a Fiberlite F9-6x1000 LEX rotor) and washed once in 1X SBG (20 mM sodium phosphate, pH 7.9; 20 mM glucose; 0.15 M NaCl). The cells were lysed at isotonic conditions by nitrogen cavitation at a cell density of ~2.0 x 10⁹ cells/mL in isotonic 1X SoTE (600 mM sorbitol, 20 mM Tris-HCl pH 7.5, 1 mM EDTA) and by applying 70 bar for 45-60 min. The mitochondrial fraction was pelleted using centrifugation (16,000 rpm, 10 min, 4°C, Sorvall SS-34 rotor) and resuspended in 1X SoTE. To remove nuclear DNA contaminations and membrane fragments, the sample was treated with DNase I (100 μg/ml) for 20-30 min on ice. In a first centrifugation (555 x g, 20 min, 4°C, centrifuge Eppendorf 5810 R with rotor A-4-81, rectangular bucket 500 mL and adaptor for five conical tube 50 mL), cell debris and living cells were separated from the mitochondrial vesicles remaining in the supernatant. The pellet was resuspended in 1X SoTE and the centrifugation was repeated to further extract mitochondrial vesicles.

In a second centrifugation run (16,000 rpm, 10 min, 4°C, Sorvall SS-34 rotor) the mitochondrial vesicles were pelleted and immediately resuspended in 1X SoTE buffer containing 50% (w/v) Nycodenz. The suspension was syringed to the bottom of precast Nycodenz step gradients (18/21/25/28% (w/v) Nycodenz in 1X SoTE buffer; capacity 3.5-8 x 10¹⁰ cells) using a Sanitex Eterna Matic syringe. The gradients were centrifuged at 27,000 rpm for 45 min at 4°C in a SW32 Ti rotor (Beckman Coulter). Mitochondrial vesicles

accumulated at the borders between 21% and 25% (w/v) Nycodenz and were harvested using a syringe. Starting with 20 L of cell culture ($3.5\text{--}5 \times 10^7$ cells/ml) usually yielded in ~ 10 g wet weight of mitochondrial vesicles.

Native *T. brucei* mitoribosome purification

Mitochondrial vesicles (approx. 12 ml) were thawed on ice and pelleted by centrifugation (20,800 x g, 10 min, 4°C). The pellet was resuspended in an equal volume (12 ml) of lysis buffer (40 mM HEPES-KOH pH 7.4, 5 mM Na₂H/NaH₂ PO₄ pH 7.4, 100 mM KCl, 10 mM MgCl₂, 3% (w/v) DDM, 2 mM DTT, 2.5 mM EDTA 10 μM bestatin, 2 μM E-64, 10 μM leupeptin, 1 μM pepstatine, 10 μM phenanthroline, 100 μM PMSF, 20 U/ml RiboLock (ThermoFisher Scientific), 125 μM spermine, 125 μM spermidine) and mitochondria were lysate by gentle mixing for 40 min at 4°C. The sample was centrifuged twice (20,800 x g, 25 min, 4°C) to clear the lysate. The cleared lysate was loaded onto a 60% (w/v) sucrose cushion in lysis buffer and centrifuged (65,000 rpm, 20 h 40 min, 4°C) using MLA-80 rotor (Beckman-Coulter). The pellets were then resuspended in 125 μl resuspension buffer (40 mM HEPES-KOH pH 7.4, 5 mM Na₂H/NaH₂ PO₄ pH 7.4, 100 mM KCl, 10 mM MgCl₂, 2 mM DTT, 0.01% (w/v) DDM) for 75 min at 4°C by gentle mixing. The sample was again cleared by centrifugation (20,800 x g, 10 min, 4°C). The supernatant was subsequently loaded onto a 10%–40% (w/v) sucrose gradient in resuspension buffer and centrifuged (45,000 rpm, 1 h 30 min, 4°C) using a SW55 Ti rotor (Beckman-Coulter). The sample was manually fractionated from the top into 13 equal fractions. Fractions 4–6 were combined and buffer-exchanged to resuspension buffer in a tabletop centrifuge at 4°C using centrifugal filters (Amicon) until the calculated sucrose concentration was below 1%.

Cryo-EM sample preparation and data acquisition

The buffer-exchanged sample was diluted 3 x with resuspension buffer to a final RNA concentration of 80 ng/μl. Quantifoil grids (R 2/2) were coated with a thin layer of carbon and glow discharged for 15 s at 15 mA. The sample (3.5 μl) was applied onto the grid, immediately blotted for 7–9 s using a Vitrobot Mark IV (Thermo Fisher Scientific) at 100% humidity and 4 °C and plunge frozen in a liquid ethane–propane mix cooled to liquid nitrogen temperature.

The cryo-EM data of the LSU native sample was collected on a Titan Krios cryo-transmission electron microscope (Thermo Fisher Scientific) equipped with a Falcon III direct electron detector (Thermo Fisher Scientific) and operating at 300 keV. Two datasets of 14,303 and 15,757 micrographs, respectively, were automatically collected using the EPU software (Thermo Fisher Scientific). A stack of 24 images was recorded for each micrograph at a defocus range between -1 to -3 μm. The exposure time was 1.3 s and the calibrated magnification was 129,000x (corresponding to a pixel size of 1.085 Å/pixel on the object scale), resulting in a total electron dose of ~ 75 electrons/Å².

Cryo-EM data processing of the mitoribosomal sample

Both datasets were collected and initially processed independently. Movie frames of both datasets were drift-corrected and dose-weighted using MotionCor2 (Zheng et al., 2017). GCTF (Zhang, 2016) was used to estimate the CTF parameters of non-dose-weighted and drift-corrected micrographs. Based on the power spectra, 13,503 and 13,273 micrographs, respectively, were selected for further processing. Subsequent data processing was carried out using Relion 3 (Zivanov et al., 2018), unless specified differently. 1,243,430 and 1,237,180 particles from dataset I and dataset II, respectively, were picked by a template-free auto-picking procedure based on a Laplacian-of Gaussian (LoG) filter. Initial 2D classification was used in processing of both datasets to remove featureless particles. Selected particles from dataset I, which was processed first, were subjected to another round of 2D classification, from which particles in LSU-like looking class averages were selected. A limited number of 2D classes were used for *ab-initio* model creation. One class of 3D *ab-initio* model creation showed an LSU-like map, with the central protuberance (CP) region missing and additional density at the ribosomal intersubunit side. This map, lowpass filtered to 50 Å, was used in 3D classification of particles from both datasets. Classes lacking an obvious density for the CP region and characterized by the additional density at the intersubunit side of the subunit were selected from both datasets and merged together, which resulted in 131,101 particles (5.3% of the starting particles). Joined particles were aligned using 3D refinement and submitted to a skip-alignment 3D classification focused on the CP region and bottom of the subunit (in the crown view) – two regions which in the refined map showed highly variable density. The classification resulted in one class representing the state A assembly intermediate, two classes representing unidentified states and the remaining classes, representing highly similar state B structures. State A contained 16,215 particles and subsequent refinement and postprocessing yielded a map resolved at 3.9 Å resolution. State B contained 98,508 particles and with following refinement, postprocessing and particle CTF refinement was resolved at 3.1 Å resolution. Two classes representing unidentified states were merged and subjected for another skip-alignment 3D classification with a focus mask around the CP region that showed the highest flexibility in the density. This classification resulted in four meaningful classes (out of 6 in total), which upon further individual refinement resulted in low resolution (9–13 Å) maps that seem to represent assembly intermediates at different stages, although the low resolution of these reconstructions prevented any further and detailed interpretation. For the processing scheme see [Figures S1](#) and [S2](#) for the quality of the cryo-EM map.

Model building and refinement

Published models for the proteins and rRNA of the previously published LSU (Ramrath et al., 2018) were docked into the cryo-EM maps using UCSF ChimeraX (Goddard et al., 2018) and adjusted in Coot (Emsley et al., 2010). Remaining unassigned densities

was addressed manually. Initially, proteins were traced as poly-alanine chains and side chain densities were used to assign the most probable amino acid sequence, considering secondary structure and local chemical environment. The obtained partial sequences were subsequently used to search through the non-redundant protein sequence database of TriTrypDB (Aslett et al., 2010) or NCBI (Altschul et al., 1990) to identify the proteins. Phyre2 (Kelley et al., 2015) was utilized to obtain model structures based on amino acid sequence homology. For most of the identified proteins, Tb427 Lister strain amino acid sequences could be used. However, for some proteins the highly homologous sequence of Tb927 strain was taken due to sequence incompleteness in the Tb427 Lister strain (Table S1). The correct fit of the side chain densities was used for validation of the identified sequence. Sequence (BLAST by NCBI) or secondary structure (PDBFold by EMBL-EBI) was used to identify homologous proteins. Most parts of the maps showed high-quality EM density features, which allowed an atomic interpretation. In some peripheral areas fragmented EM density with lower local resolution was observed, which impeded protein identification, and some stretches in well-ordered areas were too short for confident sequence assignment. These protein fragments were built as unassigned UNK residues. Similarly, areas of weaker EM density clearly encompassing rRNA features such as helices, stem-loops or single-stranded connections but unresolved base orientations were built as unassigned phosphate backbone. In the case of the H91-92 stemloop, in which the orientation, but not the identities of the bases could be established, the model was truncated to poly-pyrimidine.

The build models were initially corrected, completed and refined manually using Coot (Emsley et al., 2010). The final models were then subjected to five cycles of real space refinement using Phenix (Afonine et al., 2018), during which RNA base pair, RNA stacking, protein secondary structure, side chain rotamer and Ramachandran restraints were applied (Table 1). Using available high-resolution structures as guides, additional bond and angle restraints were imposed for some ligands, such as the coordinated zinc ions, covalently linked phosphopantetheine moieties as well as the GTPs with a hexa-coordinated magnesium. The model geometry was validated using MolProbity. Real space correlation coefficients (CC_{mask}) between cryo-EM maps and the models were calculated to evaluate the fit. Further, the model versus map FSCs at the FSC = 0.5 criterion resulted in similar resolutions as those calculated from both map half-sets at the FSC = 0.143 criterion for both models.

Northern Analysis for mitochondrial rRNAs

The Northern analysis for mitochondrial 9S and 12S rRNAs steady-state levels was done as described in Saurer et al. (2019) and basically follows the acid guanidinium thiocyanate-phenol-chloroform RNA extraction method (Chomczynski and Sacchi, 1987). RNAi cell lines were grown in triplicates in the presence of absence of tetracycline. A minimum of 5×10^7 cells were harvested for each time point and washed with 1x PBS (phosphate buffered saline). Cell pellets were dissolved immediately in 4 M guanidinium isothiocyanate containing 200 mM sodium acetate pH 4.0, 25 mM sodium citrate, 0.5% (w/v) sodium N-lauroyl sarcosinate and 100 mM β -mercaptoethanol as well as 20 mg/mL oyster glycogen. The RNA was extracted and precipitated using 1.2 volumes of ice-cold isopropanol, and pellets were washed with 70% (v/v) ethanol. 5 μ g RNA containing 0.1% (w/v) ethidium bromide were separated in 1% (w/v) agarose gels containing 200 mM formaldehyde for 1 h 45 min at 100 V. The running buffer (20 mM MOPS, 8 mM sodium acetate, 1 mM EDTA, 200 mM formaldehyde, pH 7.0) was pumped continuously between the anode and cathode reservoirs using a peristaltic pump or subjected to interval mixing. The three prominent cytosolic rRNAs (2251, 1864 and ~1400 nt) were visualized and served as loading control. A capillary blot transferred the RNA onto a charged nylon membrane for ca. 16 h in 10x SSC (130 mM NaCl, 150 mM sodium citrate, pH 7.0). The membrane was UV-crosslinked (150 mJ/cm²) and dried, followed by northern hybridization using complimentary DNA oligonucleotide probes for mitochondrial 9S and 12S rRNAs (Table S2). The membrane was pre-wetted in 0.2x SSPE (1.5 mM NaCl, 0.1 mM sodium phosphate, 0.01 mM EDTA, pH 7.4) and pre-hybridized for at least 1 h at 55°C in 10 mL of buffer containing 6x SSPE, 5x Denhardt's and 0.5% (w/v) SDS in a 51 mm diameter hybridization bottle. The buffer was discarded and the membrane was hybridized for 12-18 h at 55°C with 10 mL fresh buffer containing in addition 10 pmol 5'PNK- γ ³²P-ATP labeled DNA probe for the 9S rRNA. The membrane was washed three times with ~50 mL washing solution (2x SSPE, 0.5% (w/v) SDS) for 3 min. The blot was exposed for three days and quantified with a Typhoon FLA 9500 Phosphorimager, followed by re-hybridization using the DNA probe for the 12S rRNA and exposure for one day.

QUANTIFICATION AND STATISTICAL ANALYSIS

The phosphorimager images were quantified using the Image Quant TL software (version 8.1). The signal intensities were used to calculate the average from biological triplicates. The average from uninduced cells (day = 0) was set to 100 and all other averaged time points were normalized accordingly in an unbiased manner. The error bars represent the average deviation calculated with MS Excel.

The statistical analysis of the cryo-EM data processing, model building and model refinement is described in Method Details and in the Supplemental Information.

Creation of Figures

Molecular graphics and analyses were performed with UCSF ChimeraX, developed by the Resource for Biocomputing, Visualization, and Informatics at the University of California, San Francisco, with support from National Institutes of Health R01-GM129325 and the Office of Cyber Infrastructure and Computational Biology, National Institute of Allergy and Infectious Diseases (Goddard et al., 2018).